# Mouse Cortical Cellular Diversification Through Lineage Progression of Radial Glia

Lin Yang[1], Yanjing Gao[1], Ziwu Wang[1], Zhenmeiyu Li[1], Guoping Liu[1], Zhejun Xu[1], Zhuangzhi Zhang[1], Yan You[1], Zhengang Yang[1], and Xiaosu Li[*1]

[1]State Key Laboratory of Medical Neurobiology and MOE Frontiers Center for Brain Science, Institutes of Brain Science, and Department of Neurology, Zhongshan Hospital, Fudan University, Shanghai 200032, China

*Xiaosu Li: Email: lixiaosu@fudan.edu.cn

## Abstract

Cortical radial glia (RGs) sequentially generate pyramidal neurons (PyNs) and glia. In this study, we investigated the molecular logic underlying cortical cellular diversification using time-series scRNA-seq and snATAC-seq on FlashTag- or hGFAP-GFP-labeled mouse cortical progenitors across embryonic and postnatal stages. Our data revealed that RGs transition from early to late over time, sequentially producing intermediate neuronal progenitors (INPs) and intermediate glial progenitors (IGPs). While INPs expand exclusively to generate PyNs, IGPs progress from young to old, sequentially producing cortical astrocytes, oligodendrocytes, and olfactory bulb interneurons. We constructed comprehensive molecular maps that reflect cell lineage progression. Our study reveals that chromatin accessibility drives cellular diversification by restricting broadly expressed transcription factors to specific stages and cell types. For instance, *Lhx2*, which is constantly expressed in RGs across all stages, exhibits reduced DNA-binding activity as development progresses. *Lhx2* maintains neurogenic competence by establishing an active epigenetic state at neurogenic genes. As RGs transition to later stages, the chromatin regions bound by Lhx2 become inaccessible, leading to the loss of neurogenic competence and the acquisition of gliogenic competence.

## Introduction

Proper central nervous system function relies on the generation of a vast repertoire of distinct neural cell types from neural stem cells (NSCs). Both the spatial and temporal patterning of NSCs contribute to generating distinct neural cell types. Spatially, NSCs within distinct progenitor domains express unique combinations of transcription factors and produce particular types of neural cells (Jessell, 2000; Flames *et al*, 2007). Temporally, individual NSCs generate distinct types of neural cells in a stereotypical temporal order (Doe, 2017; Lin *et al*, 2021; Molyneaux *et al*, 2007). During mammalian corticogenesis, cortical radial glia (RGs) function as NSCs, sequentially producing cortical pyramidal neurons (PyNs) and glial cells (Kriegstein & Alvarez-Buylla, 2009). During early corticogenesis, cortical RGs produce radial clones of PyNs that migrate to the cortex in an inside-out order (Rakic, 2007). During late stages, RGs generate two types of cortical glia — astrocytes and oligodendrocytes — as well as olfactory bulb (OB) interneurons (Li *et al*, 2021; Yang *et al*, 2022; Merkle *et al*, 2007). Rather than sequentially activating distinct neuronal or glial-restricted stem cell pools, single-clone lineage tracing of cortical RGs demonstrates that individual RGs temporally switch their potential, sequentially producing PyNs and glial cells (Qian *et al*, 2000; Gao *et al*, 2014; Shen *et al*, 2021).

While temporal patterning of NSC identity is widely observed among species, the underlying mechanisms have been more extensively studied in invertebrates. In the Drosophila CNS, cascades of temporal transcription factors have been identified in the ventral nerve cord, central brain, and optic lobe (Konstantinides *et al*, 2022; Miyares & Lee, 2019; Bayraktar & Doe, 2013; Isshiki *et al*, 2001). These temporal transcription factors are sequentially expressed in NSCs. They mutually regulate each other by cascading activation of the next factor and repression of the previous one. Sequential expression of temporal transcription factors in Drosophila NSCs endows their daughter cells with different temporal identities. While the mechanisms of temporal patterning in Drosophila NSCs are well understood, the neurogenesis-to-gliogenesis transition in mammalian NSCs remains less well understood.

Single cell RNA sequencing (scRNA-seq) and single nucleus ATAC sequencing (snATAC-seq) are powerful tools for identifying cell identities and molecular profiles. Several recent studies have employed scRNA-seq and/or snATAC-seq to investigate

mouse cortical development (Telley *et al*, 2019; Ruan *et al*, 2021; Di Bella *et al*, 2021; Bhaduri *et al*, 2021; Rhodes *et al*, 2022). These studies have provided a comprehensive atlas of neurogenesis. However, gliogenesis has been less thoroughly explored, as few glial lineage cells were captured in these datasets. Cortical glia are generated gradually after the production of PyNs. During late corticogenesis, spanning from late embryonic to early postnatal stages, progenitors and glial cells account for less than 20% of all cortical cells, with the majority being postmitotic PyNs. Therefore, to elucidate the molecular logic underlying neurogenesis-to-gliogenesis transition and development of glial lineages, it is essential to use purified cortical progenitors or glial lineage cells for scRNA-seq and snATAC-seq.

In this study, we performed time series scRNA-seq and snATAC-seq on FlashTag (FT) and *hGFAP-GFP* labeled cortical progenitors. During neurogenic stages, PyNs were exclusively generated either directly or indirectly through intermediate neural progenitors (INPs). In contrast, during gliogenic stages, various cell types were produced simultaneously. Distinct subpopulations of RGs were responsible for neurogenesis and gliogenesis. Gliogenic RGs generated a common population of intermediate glial progenitors (IGPs), which transition from young to old over time, sequentially expressing combinatorial gene sets and opening distinct chromatin regions to sequentially generate cortical astrocytes, oligodendrocytes, and olfactory bulb (OB) interneurons. We established comprehensive molecular maps for cortical lineage commitment and cellular diversification, linking gene modules to specific cell fates and differentiation stages, with molecular developmental trajectories that mirror cell lineage trajectories. Our scRNA-seq and snATAC-seq data revealed that the transcriptome and epigenome in cortical RGs were temporally dynamic, coordinating the temporal neurogenesis-to-gliogenesis switch. By screening genes with temporally dynamic activity, we identified *Lhx2* as a key temporal transcription factor that regulates the timing of the neurogenesis-to-gliogenesis switch.

## Results

### Neurogenesis-to-Gliogenesis Transition Revealed by Time-Series scRNA-seq of Mouse Cortical Development

To elucidate the temporal patterning mechanisms of mouse cortical development, we performed time-series scRNA-seq on cortical progenitors from embryonic day 13 (E13) to postnatal day 1 (P1). We employed three strategies to isolate cortical progenitors (Fig. 1A). At E13, whole cortices were isolated and dissociated into single cells. From E15 to E18, cortical progenitors were enriched using fluorescence-activated cell sorting (FACS) following 24 hours of in utero intracerebroventricular FlashTag (FT) injection. From E18 to P1, GFP-expressing cells from *hGFAP-GFP* transgenic mouse cortices were sorted using FACS. The collected cells underwent single cell 3' gene expression library construction and high-throughput sequencing on an Illumina platform (Fig. 1A). Additionally, two E14 cortical samples from a published study were included (Noack *et al*, 2022). In total, 25276 cells from the neurogenic stages (E13-E15) and 40090 cells from the gliogenic stages (E17-P1) were recovered, representing the neurogenic and gliogenic dataset, respectively (Fig. 1D).

Cell type identities were determined based on the expression of well-known marker genes (Fig. 1B, C, F and Table S1). During the neurogenesis stages, *Pax6*+/*Sox2*+ cortical RGs exclusively produced *Eomes*+/*Neurog2*+ INPs. The INPs either directly differentiated into *Nueord6*+ PyNs (direct neurogenesis) or transformed into cycling INPs (cINP), which underwent 1-2 rounds of proliferation to produce PyNs (indirect neurogenesis) (Fig. 1B, E and F) (Noctor *et al*, 2004). During the gliogenic stages, RGs produced INPs and *Olig2*+/*Egfr*+ intermediate glial progenitors (IGPs) for neurogenesis and gliogenesis, respectively. The IGPs diversified into three distinct cell types: *Aldh1l1*+ astrocytes, *Sox10*+ oligodendrocytes, and *Dlx2*+ OB interneurons (Fig. 1C, E, and G). While the number of PyN lineage cells and glial lineage cells was comparable in E18 *hGFAP-GFP* cortices, the proportion of PyN lineage cells (including INPs and cINPs) was sharply reduced in P1 *hGFAP-GFP* cortices, indicating that neurogenesis was nearly complete by P1 (Fig. 1E).

In summary, the time-series scRNA-seq of mouse cortical development revealed that RGs transition from generating neurons during early stages to producing glial cells in later stages.

**Reconstruction Lineage Differentiation Trajectories During Gliogenic Stages**

During gliogenic stages, cortical RGs simultaneously generated multiple cell types. We reconstructed lineage differentiation trajectories and estimated pseudotime on our gliogenic scRNA-seq dataset using Monocle3. Neurogenic RGs were designated as the root cell population. The two main trajectories emerging from the RGs corresponded to neurogenesis and gliogenesis respectively (Fig. 2A, B). The PyN trajectory bifurcated once: one branch progressed through post-mitotic INPs, representing direct neurogenesis, while the other passed through mitotic INPs, representing indirect neurogenesis. The glial trajectory exhibited two bifurcation points. At the first branch point, one branch corresponded to astrocyte lineage, while the other progressed through IGPs to reach the second bifurcation point. At the second branch point, the trajectory further bifurcated into two terminal branches corresponding to oligodendrocytes and OB interneurons, respectively. Compared to cells that rapidly acquire OPC identity, cells follow a longer trajectory to acquire OB interneuron identity. Additionally, in terms of pseudotime, OPCs are younger than OB interneurons (Fig. 2D). Thus, we propose that IGPs generate OPCs prior to interneurons. RNA velocity-based trajectory inference revealed similar lineage trajectories, though with the directionality between RGs and IGPs reversed (Fig. 2C).

The PyN and glia lineages were descendants of RG-3 and RG-2, respectively (Fig. 2A). Thus, rather than a common population of RGs undergone neurogenesis and gliogenesis simultaneously, distinct subpopulations of RGs gave rise to PyNs and glia, respectively. The RG-3 and RG-2 population were considered as neurogenic RGs and gliogenic RGs, respectively. Both Monocle3 and RNA velocity revealed a trajectory from RG-3 to RG-2 (Fig. 2A, C), indicating that neurogenic RGs transition into gliogenic RGs. Consistent with the neurogenic-to-gliogenic transition, the proportion of neurogenic RGs decreased over time, while the proportion of gliogenic RGs increased (Fig. S1B). Several hundred differentially expressed genes were identified between neurogenic and gliogenic RGs (Fig. S1A). As expected, Gene Set Enrichment Analysis (GSEA) revealed that the GO term ‘gliogenesis’ was enriched in RG-2 (Fig. S1C-D). The GO term ‘regulation of mitotic cell cycle’ was enriched in RG-3, indicating that neurogenic RGs were more proliferate than gliogenic RGs at this stage (Fig. S1C-D).

Proliferation patterns differed between INPs and IGPs. Newly-born INPs entered a prolonged quiescent stage before initiating proliferation. In contrast, IGPs were

capable of proliferation rapidly after their generation (Fig. S1E-G). While total RNA counts and total gene counts per cell increased at a later stage along the PyN lineage pseudotime, they were rapidly increased in newly generated IGPs (Fig. S1H). Differences in the rate of gene product accumulation between INPs and IGPs may account for their distinct proliferative behaviors.

In summary, during late corticogenesis, while some cortical RGs continue to produce neurons, others transition to gliogenesis (Fig. 2E). Along the PyN lineage trajectories, the asymmetrical division of cortical RGs generates INPs, which either directly differentiate into PyNs (direct neurogenesis) or undergo a few rounds of divisions before producing PyNs (indirect neurogenesis). Along the glial lineage trajectories, asymmetrical division of cortical RGs gives rise to IGPs, which rapidly proliferate to expand the IGP pool. IGPs then divide asymmetrically several times, simultaneously self-renewing and sequentially producing cortical astrocytes, oligodendrocytes, and olfactory bulb (OB) interneurons.

### Establishing the molecular map of PyN cell fate commitment

To establish a panoramic molecular map of PyN cell fate commitment, we performed a genome-wide screen for genes dynamically expressed along the PyN lineage pseudotime. Cells associated with the neurogenic trajectories were isolated and designated as the PyN lineage (Fig. 3A-B). Gene expression levels were fitted against ranked PyN lineage pseudotime using a generalized additive model (GAM) to identify genes dynamically expressed during PyN lineage differentiation. A total of 777 genes exhibited dynamic expression along the PyN lineage pseudotime (Fig. 3C-D). These dynamically expressed genes were clustered into six modules based on their co-expression patterns (Fig. 3E and Table S2). Based on the landmark genes in each module, we designated the gene modules as 'fate determination', 'fate specification', 'proliferation', 'migration', and 'maturation'. The gene modules were spatially arranged into two trajectories corresponding to direct neurogenesis and indirect neurogenesis, which was similar to the PyN lineage trajectories. The gene modules followed a sequential order of ‘fate determination—fate specification—migration—maturation’, consistent with the PyN differentiation process (Fig. 3E) (Noctor *et al*, 2004). Aggregate expression of all genes in each module showed that each module was expressed at specific pseudotime points (Fig. 3F-G). Genes within

the same module exhibited similar expression patterns, suggesting that they may work coordinately to contribute to the same developmental events (Fig. 3H).

### Establishing the molecular map of glial lineage diversification

Cells associated with the gliogenic trajectories—from the root cell to the three terminal endpoints corresponding to astrocytes, oligodendrocytes, and OB interneurons—were isolated and designated glial lineage (Fig. 4A). Genes that were preferentially expressed in a specific lineage or dynamically expressed along the lineage pseudotime (Fig. 4C) were selected to establish a molecular map of glial lineage diversification. A total of 617 genes were clustered into 7 gene modules (Fig. 4B and Table S2). Aggregated expression levels of individual modules showed that the gene modules were specifically expressed in distinct cell types (Fig. 4D-R). We named the gene modules after their corresponding cell types (Fig. 4B). The spatial adjacency between IGP module and OL/IN-OB module was consistent with their cell lineage relationship. However, the As module was aberrantly positioned away from the IGP module, which was inconsistent with their lineage relationship. The RG & As module, which included genes expressed by both RGs and astrocytes, was positioned between the RG module and the As module (Fig. 4C). Numerous genes shared between RGs and astrocytes may influence the spatial distribution of the gene modules, potentially explaining the inconsistency between cell lineage trajectories and gene module trajectories. Genes within the same module were similarly expressed along the lineage pseudotime, which allowed for the identification of novel lineage markers (Fig. 4F).

To identify putative lineage driver genes contributing to glia lineage diversification, we systematically analyzed dynamic gene expression patterns along glia lineage trajectories. The glia lineage trajectories suggested that IGPs diversified into distinct cell types at the branch points (Fig. 2A). We hypothesized that a lineage driver gene should be able to promote IGPs to progress through the branch point towards a specific cell fate. We proposed two criteria for identifying lineage driver genes: specific expression in a particular lineage and expression preceding cell fate determination. Certain lineage marker genes, such as *Aldh1l1*, *Sox10*, and *Dlx2*, were excluded because their expression occurs only after cell fate determination (Fig. S2C). Thus, genes with lineage-biased gene expression at the branch points were

identified as putative lineage driver genes. *Hes1*, *Olig1/2,* and *Gsx2, were* identified as putative lineage driver genes for astrocytes, oligodendrocytes, and OB interneurons respectively (Fig. S2A), consistent with previous studies (Wu et al. 2003; Q. Zhou, Choi, and Anderson 2001; Q. Zhou and Anderson 2002; Silbereis et al. 2014; Waclaw et al. 2009; Chapman et al. 2018). The consistency between our screening results and previous studies indicates that our analysis method is both reliable and sensitive.

We also identified other novel putative lineage driver genes (Fig. S2A-C). *Hes1*, *Id1* and *Gli3* were identified as putative astrocyte lineage driver genes that promoted IGP progression through the first bifurcation point towards an astrocyte fate. Astrocytes share many molecular features with RGs. However, most of these genes are downregulated at the branching point when astrocyte fate is determined, excluding them from playing a role in astrocyte fate choice. *Hes1*, *Id1* and *Gli3* are among the few genes specifically expressed in the astrocyte lineage that remain active at the branch point. As transcriptional repressors, they likely determine astrocyte fate by inhibiting genes involved in oligodendrogenesis or interneuronogenesis. As the lineage trajectory progresses, the expression of *Hes1*, *Id1* and *Gli3* is extinguished in late IGPs, thereby initiating oligodendrogenesis and interneuronogenesis. At the second bifurcation, *Olig1*, *Olig2*, *Map3k1*, *Dll1*, *Dll3* and *Asdrl3* expression promotes oligodendrocyte fate, while *Gsx2*, *Gadd45g*, *Helt, Rgs16* and *Lrp8* expression favors an OB interneuron fate. Some of the putative lineage driver genes were specifically expressed in the corresponding cell types of adult mouse and human cortices (Fig. S2D) (Zhou *et al*, 2020; Saunders *et al*, 2018), further supporting their roles in lineage diversification. Thus, IGPs transition from young to old over time, sequentially expressing combinatorial gene sets to sequentially generate cortical astrocytes, oligodendrocytes, and OB interneurons.

### Temporal dynamic gene expression in mouse cortical radial glia

Cortical RGs may temporally express distinct genes to endow daughter cells with different temporal identities. To identify temporal dynamic expression genes in cortical RGs, the expression matrices associated with cortical RGs were subset from the time-series scRNA-seq dataset and our previously published cortical scRNA-seq data (Li *et al*, 2021). A total of 17000 RGs were recovered from 14 samples,

including eight timepoints spanning E13 to P2. After filter out genes with low expression at any timepoints or with small variance, a total 2656 genes were identified as RG temporal dynamic expression genes. To reveal the dynamic gene expression patterns, we applied soft clustering to these genes based on their expression levels using the fuzzy c-means algorithm. We identified 12 distinct clusters of temporal expression patterns (Fig. S3A-B). Clusters 3, 7, and 8 were downregulated over time (612 genes), while Clusters 6, 11, and 12 were upregulated (972 genes). The remaining six clusters exhibited oscillatory patterns (Fig. S3A-band Table S3). GO enrichment analysis revealed that temporally downregulated genes (early RG genes) were primarily involved in the cell cycle, RNA splicing, and chromatin remodeling. Conversely, temporally upregulated genes (late RG genes) were mainly involved in protein localization, cell junction organization, and gliogenesis (Fig. S3C). Notably, some of the temporally downregulated and upregulated genes were specifically expressed during the neurogenic and gliogenic stages, respectively (Fig. S3D).

**Temporal dynamic chromatin accessibility in mouse cortical radial glia.**

To uncover the mechanisms underlying the temporal dynamic gene expressions in cortical RGs, we accessed changes in the genome-wide organization of Accessible chromatin regions (ACRs) between early and late RGs. ACRs, which provide physical binding sites for transcription factors and the general transcription machinery, are crucial for gene expression regulation (Klemm *et al*, 2019). We performed snATAC-seq on all E13 cortical cells. The E13 cortical snATAC-seq data were integrated with our previously published snATAC-seq of the E18 FASC sorted *hGFAP-GFP* expressing cells (Li *et al*, 2021). Publicly available snATAC-seq data from E14 (Noack *et al*, 2022) and adult cortices (10x Genomics) were also included in the analysis.

The cell types identified in the snATAC-seq dataset were largely comparable to those in our scRNA-seq datasets, with the exception of the missing cINP clusters (Fig. 5A). While cell cycle genes exhibited cell type-specific expression, ACRs around them were detected similarly across all cell types, potentially accounting for the absence of the cINP population in the snATAC-seq dataset (Fig. S4A). Cell type-specific ACRs were identified to determine cluster identities (Fig. S4A and Table S4). The glial

lineage trajectories reconstructed from the E18 hGFAP-GFP snATAC-seq data revealed that IGPs first produce astrocytes, followed by oligodendrocytes and olfactory bulb (OB) interneurons, consistent with the glial lineage trajectories inferred from the scRNA-seq data (Fig. 5A).

Among the total 365211 snATAC-seq peaks, 5946 peaks were significantly more accessible and 3741 peaks were less accessible in the E18 RGs compared with E13 RGs (Fig. 5C and Table S4). The majority of the ACRs were the consistent between E13 and E18 RGs, with changes at specific locus. For example, the *Hat1* locus was temporally less accessible and the *Gfap* locus was temporally more accessible; the changes in chromatin accessibility of those genes were consistent with their developmental mRNA expression in cortical RGs (Fig. 5D).

Each cell type opens specific chromatin regions, providing specific binding sites for particular transcription factors. We computed transcription factor motif activities in each cell based on the ACRs. Cell type specific motifs were identified (Table S4), with motif activities for key transcription factors such as *Pax6*, *Olig2*, *Sox10*, *Sp9*, and *Neurog2* detected in the expected cell types (Fig. S4B). Notably, our analysis of overrepresented motifs in differentially accessible peaks between E13 and E18 radial glia (RGs) revealed a temporal shift from AT-rich to GC-rich motif activities (Fig. 5E, S4C). The *Lhx2* motif, one of the top enriched motifs in E13 RG-specific ACRs, was downregulated over time, as its target ACRs became less accessible (Fig. 5F), despite the relatively stable mRNA expression in RGs across all stages (Fig. 5G). This discrepancy in temporal trends between *Lhx2* mRNA levels and motif activity makes *Lhx2* an intriguing candidate for investigating its role in regulating neurogenesis-to-gliogenesis transition in cortical RGs (see below).

### IGPs Sequentially Open Distinct Chromatin Regions for Binding Cell Fate-Determining Transcription Factors

Our snATAC-seq data revealed that distinct cell types open specific chromatin regions, enabling the binding of transcription factors associated with cell fate determination. To identify putative transcription factors that specify each cell fate in the glial lineage, we analyzed transcription factor motif activities along the glial lineage trajectory.

Motif activities for genes such as *Sox10* and *Dlx5* were specifically detected in oligodendrocytes and OB interneurons, consistent with their expression patterns (Fig. 6H and J). Interestingly, we also observed many genes that are broadly expressed but exhibit lineage-specific motif activity. For example, while the mRNAs of *Nfia, Rorb, Nfib,* and *Rbpj* are detected in all glial lineage cells, their motif activities are restricted to the astrocyte lineage (Fig. 6A-D). Motif activities of *Nfia, Rorb*, and *Nfib* were specifically detected in young IGPs around the astrocyte bifurcation points, suggesting their roles as astrocyte fate determinants. In contrast, *Rbpj* motif activity was primarily detected in RGs and astrocytes but not in young IGPs at the astrocyte bifurcation points, indicating its role in maintaining RG and astrocyte identity rather than determining astrocyte fate. *Sox2* motif activity was detected in both young and old IGPs, while *Ascl1, Olig2*, and *Tcf4* motif activities were observed in old IGPs after the production of astrocytes (Fig. 6E-G). *Ascl1* motif activity was detected at similar levels in oligodendrocyte and OB interneuron lineages, whereas *Olig2* motif activity was higher in cells progressing toward oligodendrocytes, and *Tcf4* motif activity was higher in cells progressing toward OB interneurons. Additionally, Smad2 and Meis2 motif activities were specific higher in oligodendrocytes and OB interneurons, respectively (Fig. 6I, K).

Motifs containing the core sequences CAGCTG|CACCTG|CAGGTG|ACAATG, GGAA|TCA-TCA, and GATA|TTGT were enriched in IGPs, astrocytes, and oligodendrocytes, respectively. Furthermore, AT-rich motifs were specifically enriched in OB interneurons (Fig. 6L).

Collectively, these findings indicate that young IGPs open chromatin regions to allow the binding of *Nfia, Rorb*, and *Nfib*, thereby specifying astrocyte fate. In contrast, old IGPs open chromatin regions for the binding of *Olig2* and *Tcf4*, driving the generation of oligodendrocytes and OB interneurons (Fig. 6M).

### *Lhx2* regulated neurogenesis-to-gliogenesis switch during mouse cortical development.

Our snATAC-seq data suggest that ACRs play important roles in restricting the functions of broadly expressed transcription factors to specific periods and particular cell types. *Lhx2* could serve as a candidate gene to test whether dynamic ACRs indeed influence the temporal patterning of RGs. While scRNA-seq data show that

*Lhx2* is sustainedly expressed in both early and late RGs, snATAC-seq data reveal that *Lhx2* activity is predominantly restricted to early RGs, as its target chromatin regions become less accessible in late RGs (Fig. 5E). Early RGs predominantly produce PyNs, whereas late RGs mainly generate glial cells. If *Lhx2* functions differently in early and late RGs, the loss of *Lhx2* function could potentially disrupt the balance between neurogenesis and gliogenesis.

*Lhx2*, expressed in cortical VZ/SVZ progenitors (Fig. 7A), has been identified as a fundamental ‘‘cortical selector” gene, essential for establishing the identity of the cortical primordium(Chou & Tole, 2019). To uncover its role in the neurogenesis-to-gliogenesis switch without affecting cortical area patterning, we conditionally knocked out *Lhx2* in cortical RGs after E13.5 using *hGFAP-Cre* (*hGFAP-Cre; Lhx2*$^{F/F}$, or *Lhx2*-cKO) (Zhuo *et al*, 2001). ALDH1L1 and TNC, which are in the late RGs, their expression were barely detectable in E15.5 control cortices. However, their expressions were significantly increased in E15.5 *Lhx2*-cKO cortices (Fig. 7b). Similarly, we observed an increase in EGFR and OLIG2 expression following *Lhx2* inactivation at E15.5 and E16.5 (Fig. 6B-C). The premature expression of late-stage RGs genes (*ALDH1L1* and *TNC*) and the precocious generation of IGPs (*EGFR*+/*OLIG2*+ cells) indicated that *Lhx2* inactivation led to precocious gliogenesis. Consistent with this, neurogenesis was significantly reduced, as evidenced by decreased EOMES expression in E16.5 *Lhx2*-cKO mice (Fig. 7B). While no significant changes were observed in *FOXP1* (label Layer VI PyNs) and *BCL11b* (label Layer V PyNs) expression, *CUX1* expression (label Layer II-IV PyNs) was seriously reduced in the *Lhx2*-cKO cortex at P56 (Fig. 6C), indicating that *Lhx2* inactivation after E13.5 selectively reduced the generation of upper-layer PyNs without affecting the production of deep-layer PyNs. In summary, the conditional knockout of *Lhx2* in cortical RGs during late neurogenic stages led to the premature generation of glia at the expense of upper layer PyNs.

Upon *Lhx2* inactivation, scRNA-seq analysis of E15 FT/FACS-purified cortical progenitors from control and *Lhx2*-cKO mice confirmed a premature switch from neurogenesis to gliogenesis. A total of 9,758 cells were recovered from control cortices and 10,524 from *Lhx2*-cKO cortices. The cell types identified from the E15 control and *Lhx2*-cKO scRNA-seq data were comparable (Fig. S5A). Differentially expressed genes in each individual cell types between control and *Lhx2*-cKO mice

were identified (Fig. S5D and Table S5). Consistent with the increased *ALDH1L1* and *TNC* protein levels, their mRNA expression in RGs also increased upon *Lhx2* inactivation (Fig. S5G). Moreover, the expression of many other late RG genes was upregulated upon *Lhx2* inactivation (Fig. S5E, H, and Table S5). GO terms that were downregulated over time in cortical RGs, such as those related to RNA processing, cell cycle, and chromatin remodeling (Fig. S3F), were also downregulated upon *Lhx2* inactivation (Fig. S5F). Thus, the RGs in E15 *Lhx2* mutants displayed molecular profiles characteristic of gliogenic-stage RGs.

Defects in stem cell maintenance were observed after *Lhx2* inactivation. The proportion of RGs decreased from 19.7% in control cortices to 11.4% in *Lhx2*-cKO cortices. The expression of *Pax6* and *Hes1*, both critical for stem cell maintenance, was reduced (Fig. S5G) (Sansom *et al*, 2009; Tuoc *et al*, 2009; Hatakeyama *et al*, 2004; Ochi *et al*, 2020). The GO term 'stem cell population maintenance' was enriched in control RGs, while 'neurogenesis' was enriched in *Lhx2*-cKO RGs (Fig. S5F, H). Thus, *Lhx2* inactivation resulted in a reduction of cortical RGs due to premature neuronal differentiation.

The percentage of cycling INPs (cINP-1 and cINP-2) decreased from 35.0% in the control cortices to 20.3% in the *Lhx2*-cKO cortices (Fig. S5B-C). Additionally, cell cycle gene expression levels were reduced in RGs upon *Lhx2* inactivation (Fig. S5F). Thus, loss of *Lhx2* functions led to proliferation defects in both RGs and INPs.

In summary, *Lhx2* plays three primary roles during late neurogenesis: regulating the timing of the neurogenesis-to-gliogenesis switch, maintaining the stemness of cortical RGs, and promoting the proliferation of neuronal precursors.

### Temporal Dynamics of *Lhx2* Chromatin Binding Activities During Corticogenesis

The snATAC-seq dataset predicted a temporal downregulation of *Lhx2* motif activity in cortical RGs. To investigate changes in *Lhx2* binding activity during cortical development, we performed *Lhx2* CUT&Tag-seq on E13 and E15 cortical cells, as well as on E18 FT/FACS-purified cortical progenitors. We identified 7652, 5980, and 5768 *Lhx2* binding sites (CUT&Tag-seq peaks) at E13, E15, and E18, respectively (Fig. 8C and Table S6). The gradually reduction in the total number of *Lhx2* binding sites over time was consistent with the temporal reduction in *Lhx2* motif activity

predicted by snATAC-seq. The majority of *Lhx2* binding sites overlapped with ATAC-seq peaks (Fig. 8A and Fig. 9B), indicating that *Lhx2* tend to binding to ACRs. Approximately one-third (a total of 2249) of *Lhx2* binding sites were conserved across all three timepoints, including *Lhx2* binding sites around *Pax6*, *Notch1* and *Cux2* loci (Fig. 8A, C). Most *Lhx2* binding sites exhibited temporal dynamics, with early-stage-specific sites found at the *Unc5d* locus and late-stage-specific sites at the *Cux1* locus (Fig. 8A). At the *Unc5d* and *Cux1* loci, temporal changes in *Lhx2* binding activity were consistent with changes in chromatin accessibility, indicating that *Lhx2* binding activity is indeed influenced by chromatin accessibility (Fig. 8A). However, some consensus ACRs exhibited different *Lhx2* binding activities. At the *Auts2* locus, two ACRs with similar chromatin accessibility from E13 to E18, were bound by *Lhx2* specifically at E13 (Fig. 8A). The distinct *Lhx2* binding activities on consensus ACRs suggest that *Lhx2* binding might be regulated by mechanisms beyond chromatin accessibility. We also examined whether the DNA sequence of *Lhx2* motif changed along cortical development. The core “TAATTA” motif was present in all de novo motifs across the three timepoints, with the bases adjacent to the core motif becoming progressively more conserved over time (Fig. 8B). In summary, *Lhx2* binding activities were temporally dynamic along corticogenesis.

To access how *Lhx2* regulates its target gene expression, we performed ATAC-seq on all E15 cortical cells and on E15 FT/FASC-purified cortical progenitors from control and *Lhx2*-cKO mice. *Pax6* mRNA was most significantly downregulated upon *Lhx2* inactivation. At the *Pax6* locus, *Lhx2* non-target ACRs (ATAC-seq peaks not overlapping with *Lhx2* CUT&Tag-seq peaks) showed no change in chromatin accessibility, whereas *Lhx2* target ACRs (ATAC-seq peaks overlapping with *Lhx2* CUT&Tag-seq peaks) were significantly less accessible upon *Lhx2* inactivation (Fig. 8E). Similar changes in chromatin accessibility were observed at *Neurog2* and *Cux2* loci (Fig. 8E). We recovered 52733 ACRs from the control and *Lhx2*-cKO cortical progenitors. Among these peaks, 6905 were *Lhx2* target ACRs. Of these *Lhx2* target ACRs, 3802 (55.1%) were less accessible, 246 (3.6%) were more accessible and 41.3% (2857) were unchanged upon *Lhx2* inactivation (Fig. 8F). The ACRs with the most significantly downregulated chromatin accessibility after *Lhx2*-cKO were always identified as *Lhx2* target ACRs (Fig. 8F). Thus, *Lhx2* inactivation led to a reduction in chromatin accessibility at its target ACRs.

*Lhx2* positively regulates its target gene expression by maintaining chromatin accessibility. GO analysis of *Lhx2* target genes suggested that *Lhx2* regulates multiple aspects of cortical development, including neurogenesis, precursor proliferation, and cell fate commitment (Fig. 8D). This is consistent with the defects in cortical development observed upon *Lhx2* inactivation (Fig. S5F-H). In contrast, the GO term 'gliogenesis' was not enriched among *Lhx2* targets, and *Lhx2* rarely bound to the late RG genes. Thus, during late neurogenic stages, *Lhx2* balances neurogenesis and gliogenesis in cortical RGs by directly maintaining neurogenic competence through increasing chromatin accessibility at neurogenic, thereby sustaining the generation of upper-layer PyNs, while indirectly repressing gliogenic competence to prevent premature gliogenesis.

### Epigenetic mechanisms of gene expression regulation by *Lhx2*

To elucidate the mechanisms by which *Lhx2* regulates target gene expression, we compared the enrichment of H3K4me3, H3K27me3 and POLR2A between control and *Lhx2*-cKO cortices. H3K4me3 is an active epigenetic marker to identify active gene promoters (Heintzman *et al*, 2007). H3K27me3 is a repressive epigenetic marker and involved in silencing the expression of developmental genes (Wiles & Selker, 2017); POLR2A is the largest subunit of RNA polymerase II, which is responsible for mRNA synthesis (Mita *et al*, 1995). E15 control and *Lhx2*-cKO cortices were subjected to CUT&Tag-seq using H3K4me3, H3K27me3 and POLR2A antibodies. Histone modifications can spread across large chromatin regions from initial transcription factor binding site, while the insulator *Ctcf* creates boundaries that insulate chromatin from epigenetic modifications (Narendra *et al*, 2015). To demarcate the chromatin regions regulated by *Lhx2*, we took advantage of the CTCF ChIP-seq of P0 forebrain (GEO: GSE91978) and the *Lhx2* CUT&Tag-seq to segregate the chromatin into *Lhx2* related and *Lhx2* non-related regions (Fig. 9A).

At the *Foxp4* locus, two active promoters were identified based on the enrichment of H3K4me3 modification. One promoter was located within the *Lhx2* non-related region, while the other was located approximately 9.5 kb downstream of the *Lhx2* binding site (Fig. 9A). These promoters were designated as the *Lhx2* non-related promoter and the Lhx2 related promoter, respectively. H3K4me3 levels within the *Lhx2* non-related promoter were comparable between control and *Lhx2*-cKO mice. However,

they were significantly reduced within the *Lhx2* related promoter in *Lhx2*-cKO mice. Upon *Lhx2* inactivation, the *Lhx2* non-target ACRs within both the *Lhx2* non-related and *Lhx2*-related regions remained unaffected, whereas the *Lhx2* target ACRs exhibited decreased chromatin accessibility. Similar situation was observed at the *Pax6* locus and many other gene loci. Thus, *Lhx2* activates the promoters of its target genes by increasing H3K4me3 modification, without altering the chromatin accessibility of the *Lhx2* non-target ACRs within these promoters.

The nearest *Lhx2* binding sites were located 9.5 and 11.5 kb from the transcription start site (TSS) of *Foxp4* and *Pax6*, respectively, indicating that *Lhx2* regulates these gene promoter remotely. This remote promotor regulation is further supported by the distribution of *Lhx2* binding sites (Fig. 9B). The majority of *Lhx2* binding sites were located within the gene intron (36.9%), gene downstream (19.2%) or intergenic (22.1%) regions, while only 17.1% were located within promoter regions. Thus, *Lhx2* prefers binding to gene distal enhancers and remotely activates gene promoters.

At the *Foxp4* locus, no significant H3K27me3 enrichment was detected in the *Lhx2* non-related region of either control or *Lhx2*-cKO cortices. However, H3K27me3 levels were increased within the *Lhx2* related region of *Lhx2*-cKO cortices (Fig. 9A). This increase in H3K27me3 modification spread both upstream to the *CTCF* binding site and downstream to the accessible chromatin region (ACR) within the promoter.

*Lhx2* inactivation led to epigenetic repression specifically within the *Lhx2* related chromatin regions. Consistent with this, POLR2A levels were reduced specifically within the *Lhx2* related region upon *Lhx2* inactivation (Fig. 9A). The decrease in POLR2A levels likely resulted in reduced mRNA synthesis, which was confirmed by reduced *Foxp4* mRNA expression (Fig. S5D and Table S7).

In summary, *Lhx2* maintains an active epigenetic state of its target genes to promote their expression (Fig. 9C). First, *Lhx2* binds to distal enhancers and increases the chromatin accessibility of its target ACRs. Second, *Lhx2* remotely regulates nearby promoters through increasing H3K4me3 modification levels. Third, *Lhx2* reduces H3K4me27 levels within local and adjacent chromatin regions.

## Discussion

During cortical development, RGs transition from early to late stages, sequentially producing INPs and IGPs. While INPs exclusively differentiate into PyNs, IGPs transition from young to old, sequentially generating cortical astrocytes, oligodendrocytes, and OB interneurons. As RGs transition from early to late and IGPs progress from young to old, they sequentially express distinct genes to coordinate production of distinct cell types. Our analysis also uncovered that chromatin accessibility plays a critical role in regulating the temporal patterning of RGs and IGPs by restricting the functions of broadly expressed transcription factors to specific periods and particular cell types. We identified Lhx2 as a temporal transcription factor that epigenetically regulates the timing of the neurogenesis-to-gliogenesis transition.

Our study extends the understanding of temporal patterning by highlighting the pivotal roles of chromatin accessibility. It also raises important questions for further exploration: What mechanisms govern the temporal changes in chromatin accessibility in RGs and IGPs? How do neurogenic genes progressively lose chromatin accessibility, and how do gliogenic genes progressively gain chromatin accessibility over time?

### Mechanisms Regulating the Neurogenesis-to-Gliogenesis Transition

During late corticogenesis, a subset of cortical RGs progressively transitions from neurogenesis to gliogenesis. Previous studies regarding the mechanisms underlying neurogenesis-to-gliogenesis switch have emphasized epigenetic regulation. As corticogenesis progresses, the gliogenic genes undergo gradual DNA demethylation (Takizawa *et al*, 2001; Fan *et al*, 2005; Sanosaka *et al*, 2017), while the neurogenic genes are gradually trimethylated at H3K27 (Hirabayashi *et al*, 2009). Our findings reveal that temporal changes in chromatin accessibility play a role in regulating the neurogenesis-to-gliogenesis transition. Gliogenic genes become more accessible and neurogenic genes become less accessible in cortical RGs along development (Fig. S4a). It is likely that the epigenetic states of RGs endow them with either neurogenic or gliogenic competence.

Several extrinsic signals synergize with cell intrinsic epigenetic programs to regulate the neurogenesis-to-gliogenesis switch. Notch signaling, activated by ligands on the neighboring INPs, induces DNA demethylation of the gliogenic genes (Namihira *et al*,

2009; Bansod *et al*, 2017). SHH signaling promotes neurogenesis-to-gliogenesis switch by reducing *Gli3* repressor, which interacts with the BAF ATP-dependent chromatin remodeling complex (Zhang *et al*, 2020; Zhan *et al*, 2011). Thus, both cell intrinsic programs and extrinsic signaling molecules regulated the neurogenesis-to-gliogenesis switch.

### Cellular Diversification Along Glial Lineage Trajectories

In recent years, significant efforts have been made to uncover the molecular mechanisms underlying cellular diversification. During corticogenesis, INPs and IGPs are generated for neurogenesis and gliogenesis respectively. While INPs commit to a single lineage, differentiating exclusively into PyNs, IGPs follow multi-directional trajectories, giving rise to three distinct cell types. Analysis of glial lineage trajectories from scRNA-seq and snATAC-seq data revealed that IGPs first produce astrocytes, followed by the generation of oligodendrocytes and OB interneurons. Similar to RGs that produce PyNs and glia in a stereotypical temporal order, IGPs sequentially generate astrocytes, followed by oligodendrocytes and interneurons. Thus, the temporal patterning of both RGs and IGPs contributes to cortical cellular diversity. This concept is supported by studies of Drosophila type 2 neuroblast lineages, where NSCs and INPs generate distinct progeny as they transition from early to late stages over time (Bayraktar & Doe, 2013).

While cortical RGs transition from neurogenesis to gliogenesis, their progeny, IGPs transition from astrogenesis to oligodendrogenesis and interneuronogenesis. We hypothesize that the oligodendrogenic and interneuronogenic potential is initially silenced in the early IGP by the putative astrocyte lineage driver genes, *Hes1*, *Id1* and *Gli3*. These three transcriptional repressors are specifically expressed along the astrocyte lineage and likely determine astrocyte fate by inhibiting the expression of genes involved in oligodendrogenesis and interneurogenesis. Consistent with this, Gli3 binding activities were detected at the *Sox10*, *Olig1/2* and *Gsx2* gene loci (Hasenpusch-Theil *et al*, 2018). After astrocytes are produced, the expression of these astrocyte lineage driver genes diminishes in late IGPs, allowing the IGPs to gain oligodendrogenic and interneuronogenic competence.

The transition from astrogenesis to oligodendrogenesis and interneurogenesis in late IGPs is achieved through the removal of *Hes1*, *Id1* and *Gli3* repressor activities in

late IGPs, a hypothesis supported by several previous studies. *Hes1*, a canonical Notch effector, is induced by Notch activation. Notch signaling, activated by ligands on the neighboring INPs, induces DNA demethylation at RG/As genes in the cortical progenitors (Namihira *et al*, 2009; Guo *et al*, 2023). Conditional knockout of *Rbpj*, which inactivates Notch, results in defects in astrocyte generation but an increase in oligodendrocyte production (Guo *et al*, 2023; Taylor *et al*, 2007). Moreover, *Hes1* regulates the choice between astrocyte and oligodendrocyte fates in glial-restricted precursors in the spinal cord (Wu *et al*, 2003). *Id1* expression is induced by BMP signaling, which promotes astrocyte identity and blocks neuron/oligodendrocyte lineage commitment (Gámez, Rodriguez-Carballo, and Ventura 2013). Id proteins, which are basic helix-loop-helix (bHLH) transcription factors lacking DNA-binding domains, dimerize with bHLH factors like *Olig1/2* to inhibit their functions through sequestering those proteins from DNA binding (Samanta & Kessler, 2004; Cheng *et al*, 2007). *Gli3* repressor activities are primarily regulated by SHH signaling, with its repressor domain being removed upon Shh activation. Reduced Shh activation in cortical progenitors leads to defects in cortical oligodendrocyte and OB interneuron development, whereas overactivation of the Shh pathway induces precocious and excessive production of OB interneurons (Zhang *et al*, 2020; Liang *et al*, 2024; Winkler *et al*, 2018). Notch/BMP signaling positively regulates *Hes1*/*Id1* expression to promote astrocyte identity, while SHH signaling negatively regulates *Gli3* repressor activities to specify oligodendrocyte and OB interneuron identities.

**Bivalent epigenetic regulation modulates chromatin accessibility of *Lhx2* target ACRs**

We hypothesize that *Lhx2* target ACRs are subject to a dynamic balance between active and repressive epigenetic factors for the following reasons. First, the majority of E13 *Lhx2* target ACRs become closed in late-stage cortical RGs (e.g., the *Unc5d* locus in Fig. 7a), indicating that negative epigenetic regulation gradually surpasses the positive regulation by *Lhx2* at those ACRs. Second, *Lhx2* interacts directly or indirectly with both the NuRD and BAF complexes. Mass spectrometric analysis of *Lhx2*-interacting proteins revealed co-immunoprecipitation of NuRD subunits (Rbbp4 and Ss18l1) and BAF subunits (Smarcc1, Smarcc2, and Smarce1) with Lhx2 (Muralidharan *et al*, 2017; Nguyen *et al*, 2022). Both NuRD and BAF complexes are ATP-dependent chromatin remodeling complexes. NuRD is a transcriptional corepressor that couples ATP-dependent chromatin remodeling with histone

deacetylase activity (Nitarska *et al*, 2016; Bornelöv *et al*, 2018), while the BAF complex primarily activates gene expression by evicting nucleosomes from ACRs (Brahma & Henikoff, 2024; Narayanan *et al*, 2015). Third, *Lhx2* and Polycomb complexes exert opposing effects on the chromatin accessibility of neurogenic genes (Hirabayashi *et al*, 2009). *Lhx2* positively regulates the chromatin accessibility of neurogenic genes to maintain neurogenic competency for producing upper layer PyNs, while Polycomb complexes negatively regulate these genes to facilitate the transition to gliogenesis. Thus, a balance between positive and negative epigenetic regulation delicately controls the chromatin accessibility of *Lhx2* target ACRs.

Epigenetic factors are usually recruited to specific chromatin regions via interactions with transcription factors. At *Lhx2* target ACRs, active epigenetic factors can be recruited by *Lhx2*, which recognizes specific DNA motif. Repressive epigenetic factors are recruited to specific genes by yet unidentified factors. It is unlikely that *Lhx2* recruits both active and repressive epigenetic factors, as *Lhx2* primarily positively regulates its target ACRs. Alternatively, a putative *Lhx2* "competitor" may be required for the accurate targeting of repressive epigenetic factors, which remains to be identified in the future.

### Temporal dynamic *Lhx2* binding activities

*Lhx2* functions throughout cortical neurogenesis. At the beginning of neurogenesis, *Lhx2* promotes cortical primordium identify by repressing the hem and anti-hem fate (Chou & Tole, 2019). During early neurogenesis, it promotes the specification of layer 6 over layer 5 PyN identity (Muralidharan *et al*, 2017). During late neurogenesis, it maintains neurogenic competence for producing upper-layer PyNs and prevents premature gliogenesis. *Lhx2* plays distinct roles at different developmental stages. Consistent with its temporally dynamic roles, its DNA-binding activities exhibit developmental dynamics. *Lhx2* binds to different genes at various developmental stages. Overall, its binding activities are progressively reduced in cortical RGs over time. Several factors may affect its binding affinity. First, as *Lhx2* primarily binds to ACRs, changes in chromatin accessibility in cortical RGs influence *Lhx2* binding. Second, the *Lhx2* motif become more conserved over time, potentially contributing to the reduced *Lhx2* binding activities in cortical RGs. Third, our snATAC data revealed that the ACR around the promoter of longer *Lhx2* transcript become temporally

closed, which could lead to developmental expression of different *Lhx2* protein isoforms.

The temporally dynamic DNA-binding activities of *Lhx2* coordinate the temporal potential switch from neurogenic to gliogenic in cortical RGs. Initially, *Lhx2* binds to neurogenic genes to maintain neurogenic competence in cortical RGs. As corticogenesis progresses, *Lhx2* activities gradually decrease, leading RGs to lose neurogenic competence and transition into gliogenesis.

## Methods

### Mice

All experiments performed at Fudan University Shanghai Medical College were approved by Fudan University Animal Ethics Committee. *Lhx2*-flox mice ( Strain NO. T036697 ) were purchased from GemPharmatech (Nanjing, China). *hGFAP-Cre* mice and *hGFAP-GFP* mice were previously described (Zhuo *et al*, 2001). The transgenic mice were genotyped by PCR using the following primers: *Lhx2*, “TGGTCTAAGGATCAAGAGGCTAC”, “GCGGTTAAGTATTGGGACAGAG”; *hGFAP-Cre*, “ACGAGTGATGAGGTTCGCAAGA”, “GATTAACATTCTCCCACCGTCAGT”. The day of vaginal plug detection was designated E0.5. The day of birth was designated P0.

### Immunohistochemistry and imaging

Adult mice were perfused with 1× PBS (pH 7.4), followed by 10min 4% paraformaldehyde (PFA) in PBS. The adult brain tissues were postfixed overnight in 4% PFA. Embryonic brains were immersion fixed for 4 hours in 4% PFA. All the brain tissues were cryoprotected overnight in 30% sucrose, frozen in the embedding medium, and cryosectioned at 14/30 μm using a cryostat (CM1950, Leica, USA). The sections were first permeabilized with 0.05% Triton X-100 for 30 min, followed by incubation in blocking buffer (5% donkey serum and 0.05% Triton X-100 in TBS) for 2 h. The sections were incubated with primary antibodies overnight at 4°C. Primary antibodies were removed by washing three times with TBS. The sections were incubated with secondary antibodies for 2 hours at room temperature. The secondary antibodies were from Jackson ImmunoResearch and Invitrogen. Finally, the sections

were counterstained with DAPI for 3 min before being mounted in fluorescence mounting medium (DAKO S3023). The following primary antibodies were used: OLIG2 (1:1,000, rabbit, Millipore AB9610), OLIG2 (1:1,000, antigen retrieval, mouse, Millipore MABN50), EGFR (1:2,000, goat, R&D System AB_355937), ALDH1L1 (1:1,000, rabbit, antigen retrieval, Abcam ab10712968), BCL11B (1:1500, rat, Abcam, ab18465), EOMES (1:300, rabbit, Abcam, ab23345), EOMES (rat, 1:500, Thermo Fisher, 12-4875-82), FOXP2 (1:500, goat, Santa Cruz, sc-21 069), CUX1 (1:200, rabbit, Santa Cruz, sc-13024), TNC (1:200, rabbit, Abcam, ab108930).

The fluorescent images were taken with Olympus FV1000 confocal microscope system using a 10×,20×, or a 40× objective. Z-stack confocal images were reconstructed using the FV10-ASW software. All images were merged, cropped, and optimized in Photoshop CC without distortion of the original information.

### Cortical tissues dissociation

The embryonic cortices were dissected in ice-cold PBS and digested for 15-20 mins at 37◦C with 80 U/mL papain (sigma, p3125), 200 U/mL DNase I (Invitrogen,18047019) in DMEM cell culture medium (Gibco, 10566024). The tissues were dissociated into single cell suspension by pipetting several times. FBS containing DMEM was added to stop the enzymatic reaction. The cells were filtered with a pre-wet 40 μM cell strainer (Corning, 352340) and pelleted at 300 g (RCF) for 5 min. The cells were resuspended in 10% FBS containing DMEM. Viable cells were counted using 0.4% Trypan Blue under microscope.

### Bulk ATAC-seq

For bulk ATAC-seq, 20,000 to 50,000 cells were pelleted at 500 × g for 3 minutes. We added 20 μL of the Tn5 tagmentation mixture to simultaneously facilitate cell/nuclear membrane penetration and Tn5 tagmentation. The Tn5 tagmentation mixture consisted of 6.6 μL H2O, 7 μL PBS, 0.2 μL 10% Tween-20, 0.2 μL 1% digitonin, 4 μL 5× Tn5 buffer, and 2 μL of ME adapter sequence-loaded Tn5 transposases (Vazyme, TD501). The DNA fragments were purified using 2X VAHTS DNA Clean Beads (Vazyme, N411-01). PCR (12–15 cycles) was used to amplify the Tn5-fragmented DNA and incorporate i5/i7 adapters, sequencing primers, and sample indices for Illumina sequencing. The 200–800 bp PCR products were purified

using 0.6×/1.2× SPRIselect Reagent (Beckman Coulter, B23318) and subsequently subjected to Illumina PE150 Nova sequencing.

### CUT&Tag-seq

For CUT&Tag-seq, 1–2 × $10^5$ cells were washed with 500 μL of wash buffer and centrifuged at 600 g for 3 minutes at room temperature. The cell pellets were then resuspended in 100 μL of wash buffer. Concanavalin A-coated magnetic beads were washed twice with 100 μL of binding buffer. Next, 10 μL of the activated beads were added to the cell suspension and incubated at room temperature for 10 minutes. Following incubation, the binding buffer was removed, and the bead-bound cells were resuspended in 50 μL of antibody buffer. Subsequently, 1 μg of primary antibodies was added and the mixture was incubated overnight at 4°C. The following primary antibodies were used: Lhx2 (Abcam, ab184337), H3K4me3 (ABclonal, A22146), H3K27me3 (ABclonal, A22396), and Polr2a (BioLegend, 664906). After the removal of the primary antibody solution, 0.5 μg of the appropriate secondary antibodies were added to 50 μL of Dig-wash buffer and incubated at room temperature for 1 hour. The cells were then washed three times with Dig-wash buffer to remove any unbound antibodies. Next, the cells were incubated with 0.04 μM Tn5 transposase in 100 μL of Dig-300 buffer at room temperature for 1 hour. The cells were washed three times with Dig-300 buffer to remove any unbound transposase. The cells were then resuspended in 300 μL of tagmentation buffer and incubated at 37°C for 1 hour. To terminate tagmentation, 10 μL of 0.5 M EDTA, 3 μL of 10% SDS, and 2.5 μL of 20 mg/mL Proteinase K were added to the 300 μL sample, followed by overnight incubation at 37°C. DNA was purified using phenol–chloroform–isoamyl alcohol extraction, followed by ethanol precipitation and RNase A treatment. PCR amplification and Illumina sequencing were performed using a protocol similar to that of ATAC-seq.

### Data analysis of Bulk ATAC-seq and CUT&Tag-seq

We used Trim Galore to remove low-quality bases and adapter sequences from the FastQ files. The cleaned reads were mapped to the mouse genome GRCm39 (GENCODE, release M31) using the Subread alignment tool. PCR duplicates, unpaired reads, and reads with low mapping quality scores were filtered out from the BAM files using Sambamba and SAMtools. The cleaned BAM files were then

converted into RPKM-normalized bigWig files using deepTools. These bigWig files were visualized using IGV. Peak calling was performed on the bigWig files using LanceOtron. The peaks were annotated to the nearest genes using ChIPseeker.

For differential ATAC-peak analysis between control and *Lhx2* cKO cortical progenitors, peaks from both control and mutant ATAC-seq data were merged into common peaks using the `reduce` function in GenomicRanges. Read counts within these common peaks were obtained from the cleaned BAM files using `featureCounts` in the Rsubread package. Differential analysis of read counts was conducted using EdgeR.

The consensus and temporal dynamics of *Lhx2* binding sites were identified using Vennerable and VennStem. Overlaps between *Lhx2* CUT&Tag-seq peaks and snATAC-seq peaks were identified using the `findOverlaps` function in GenomicRanges, while overlaps between *Lhx2* CUT&Tag-seq peaks and bulk ATAC-seq peaks were determined using BEDTools intersect.

### scRNA-seq and snATAC-seq

For scRNA-seq, 1–2 × $10^4$ cells were loaded into the 10X Genomics Chromium platform to recover between 6,000 and 12,000 cells. scRNA-seq libraries were constructed using the Chromium Next GEM Single Cell 3' Reagent Kits v3.1, following the manufacturer's instructions (manual document part number: CG000205 Rev C, 10x Genomics). The cDNA libraries were then purified, quantified using an Agilent 2100 Bioanalyzer, and sequenced on an Illumina NovaSeq 6000 system.

For snATAC-seq, 2–5 × $10^5$ cells were subjected to nuclei isolation according to the manufacturer's instructions (manual document part number: CG000366 Rev D, 10x Genomics). A total of 1–2 × $10^4$ transposed nuclei were loaded to recover 3,000–6,000 cells. snATAC-seq libraries were constructed using the Chromium Next GEM Single Cell ATAC Reagent Kits v1.1, following the manufacturer's instructions (manual document part number: CG000209 Rev F, 10x Genomics). The snATAC-seq libraries were sequenced on an Illumina NovaSeq 6000 system, yielding approximately 13,000–30,000 read pairs per cell.

### Data Analysis of scRNA-seq

To generate the gene expression matrix for scRNA-seq, we used Cell Ranger count (10x Genomics Cell Ranger v7.1.0) with the mouse genome GRCm39 as the reference. The expression matrices were corrected for ambient mRNA contamination using SoupX. Low-quality cells were filtered out based on total counts, the number of detected genes, and the percentage of mitochondrial genes. Doublets were identified and removed using DoubletFinder. Cells not belonging to cortical radial glial (RG) lineages were also excluded. The cleaned count matrices were merged into two datasets corresponding to neurogenesis and gliogenesis. Seurat objects were created from these datasets The data were log-normalized and scaled, with cell cycle genes and mitochondrial genes regressed out. Principal component analysis (PCA) was performed, and batch effects were corrected using Harmony integration. UMAP dimensionality reduction and clustering were then performed on the Harmony-integrated PCs. Differential expression analysis between neurogenic and gliogenic RGs was conducted using both EdgeR and presto.

The count matrix specific to cortical RGs was subset from the scRNA-seq datasets. Counts were normalized by sequencing depth for each cell. Genes with low expression across all time points (max mean < 0.3) were filtered out. To generate the age-related gene expression matrix, we computed the average gene expression at each time point, ordering them by age. Genes with minimal variation (standard deviation > 0.2) were also filtered out. Gene temporal dynamic patterns were clustered using Mfuzz. Gene Ontology (GO) enrichment and Gene Set Enrichment Analysis (GSEA) were performed using ClusterProfiler, with similar GSEA GO terms grouped using aPEAR.

The Seurat object was converted into Monocle object to reconstruct lineage trajectories and infer cell pseudotime (https://cole-trapnell-lab.github.io/monocle3/). Genes differentially expressed along the pyramidal neuron (PyN) or glial lineage trajectories were identified using the Moran's I test. Expression levels for each gene were fitted with the lineage pseudotime using the generalized additive model (GAM) in the mgcv package, and fitted values were extracted. Pseudotime-dynamic genes were identified using Mfuzz and clustered into co-expression modules.

Unspliced and spliced reads were annotated using Velocyto, which distinguishes between nascent pre-mRNA and mature mRNA in scRNA-seq datasets. Cellular dynamics were inferred from mRNA splicing kinetics using scVelo.

### Data Analysis of snATAC-seq

The Cell Ranger ATAC pipeline (v2.1.0) was used to process the FastQ files from snATAC-seq. To combine snATAC-seq datasets across all time points, a common set of distinct, non-overlapping peaks was created by merging all intersecting peaks using the reduce function in GenomicRanges. Counts within these common peaks were quantified for each cell to create Signac objects for each sample. The Signac objects were then merged and annotated with mouse genome annotation GRCm39-M31. Cells were filtered based on total counts, nucleosome signal, TSS enrichment, and peak enrichment. The Signac object underwent TF-IDF normalization, Latent Semantic Indexing (LSI) dimensional reduction, UMAP reduction, and clustering. Cell type-specific peaks were identified, and differential peak analysis between E13 and E18 RGs was performed using both EdgeR and presto.

Motif activities per cell were calculated using motifs from mouse transcription factors and chromatin regulators, which were downloaded from JASPAR, CIS-BP, Homer, and HOCOMOCO (Raulusevicіute *et al*, 2024; Weirauch *et al*, 2014; Vorontsov *et al*, 2024). After filtering motifs with low information content (IC) scores and merging similar motifs associated with the same genes, a total of 2,858 motifs related to 1,200 genes were retained. Per-cell motif activity scores were computed using chromVAR, and cell type-specific motif activities were identified.

### Acknowledgments

This study was supported by the Ministry of Science and Technology of China (STI2030-2021ZD0202300), National Natural Science Foundation of China (NSFC 31820103006, 32070971, 32100768, 32200776, and 32200792), Shanghai Municipal Science and Technology Major Project (No. 2018SHZDZX01), ZJ Lab, and Shanghai Center for Brain Science and Brain-Inspired Technology.

### Author contributions

X.L. designed research. L.Y. performed research. Y.G., Z.W., Z.L., G.L., Z.X., Y.Y., Z.Y., and X.L. contributed new reagents/analytic tools; X.L. performed data analysis and wrote the paper.

## Disclosure and competing interest statement

All authors declare that they have no competing interests.

## Data availability

scRNA-seq, snATAC-seq, Bulk ATAC-seq, Cut&Tag-seq data used in this study have been deposited in the Gene Expression Omnibus (GEO) and are accessible through GEO Series accession number GSE276209. The E14 cortical scRNA-seq was from previous studies (GSE155677) (Noack *et al*, 2022). scRNA-seq data of E18 FT/FACS cortical progenitors (GSE221389) and snATAC-seq data of E18 *hGFAP-GFP* cortical progenitors (GSE161132) was used in our previous studies (Li *et al*, 2021, 2023). The code used for generating the data and all the figures are available under https://github.com/xiao00su/temporal.

## References


Bansod S, Kageyama R & Ohtsuka T (2017) Hes5 regulates the transition timing of neurogenesis and gliogenesis in mammalian neocortical development. *Development* 144: 3156–3167

Bayraktar OA & Doe CQ (2013) Combinatorial temporal patterning in progenitors expands neural diversity. *Nature* 498: 449–455

Bhaduri A, Sandoval-Espinosa C, Otero-Garcia M, Oh I, Yin R, Eze UC, Nowakowski TJ & Kriegstein AR (2021) An atlas of cortical arealization identifies dynamic molecular signatures. *Nature* 598: 200–204

Bornelöv S, Reynolds N, Xenophontos M, Gharbi S, Johnstone E, Floyd R, Ralser M, Signolet J, Loos R, Dietmann S, *et al* (2018) The Nucleosome Remodeling and Deacetylation Complex Modulates Chromatin Structure at Sites of Active Transcription to Fine-Tune Gene Expression. *Mol Cell* 71: 56-72.e4

Brahma S & Henikoff S (2024) The BAF chromatin remodeler synergizes with RNA polymerase II and transcription factors to evict nucleosomes. *Nat Genet* 56:

100–111

Chapman H, Riesenberg A, Ehrman LA, Kohli V, Nardini D, Nakafuku M, Campbell K & Waclaw RR (2018) Gsx transcription factors control neuronal versus glial specification in ventricular zone progenitors of the mouse lateral ganglionic eminence. *Dev Biol* 442: 115–126

Cheng X, Wang Y, He Q, Qiu M, Whittemore SR & Cao Q (2007) Bone Morphogenetic Protein Signaling and Olig1/2 Interact to Regulate the Differentiation and Maturation of Adult Oligodendrocyte Precursor Cells. *Stem Cells* 25: 3204–3214

Chou S-J & Tole S (2019) Lhx2, an evolutionarily conserved, multifunctional regulator of forebrain development. *Brain Res* 1705: 1–14

Di Bella DJ, Habibi E, Stickels RR, Scalia G, Brown J, Yadollahpour P, Yang SM, Abbate C, Biancalani T, Macosko EZ, *et al* (2021) Molecular logic of cellular diversification in the mouse cerebral cortex. *Nature*

Doe CQ (2017) Temporal Patterning in the Drosophila CNS. 25

Fan G, Martinowich K, Chin MH, He F, Fouse SD, Hutnick L, Hattori D, Ge W, Shen Y, Wu H, *et al* (2005) DNA methylation controls the timing of astrogliogenesis through regulation of JAK-STAT signaling. *Development* 132: 3345–3356

Flames N, Pla R, Gelman DM, Rubenstein JLR, Puelles L & Marín O (2007) Delineation of Multiple Subpallial Progenitor Domains by the Combinatorial Expression of Transcriptional Codes. *J Neurosci* 27: 9682–9695

Gámez B, Rodriguez-Carballo E & Ventura F (2013) BMP signaling in telencephalic neural cell specification and maturation. *Front Cell Neurosci* 7

Gao P, Postiglione MP, Krieger TG, Hernandez L, Wang C, Han Z, Streicher C, Papusheva E, Insolera R, Chugh K, *et al* (2014) Deterministic Progenitor Behavior and Unitary Production of Neurons in the Neocortex. *Cell* 159: 775–788

Guo R, Han D, Song X, Gao Y, Li Z, Li X, Yang Z & Xu Z (2023) Context-dependent regulation of Notch signaling in glial development and tumorigenesis. *Sci Adv*

Hasenpusch-Theil K, West S, Kelman A, Kozic Z, Horrocks S, McMahon AP, Price DJ, Mason JO & Theil T (2018) Gli3 controls the onset of cortical neurogenesis by regulating the radial glial cell cycle through *Cdk6* expression. *Development* 145: dev163147

Hatakeyama J, Bessho Y, Katoh K, Ookawara S, Fujioka M, Guillemot F & Kageyama R (2004) *Hes* genes regulate size, shape and histogenesis of the nervous system by control of the timing of neural stem cell differentiation. *Development* 131: 5539–5550

Heintzman ND, Stuart RK, Hon G, Fu Y, Ching CW, Hawkins RD, Barrera LO, Van Calcar S, Qu C, Ching KA, *et al* (2007) Distinct and predictive chromatin signatures of transcriptional promoters and enhancers in the human genome. *Nat Genet* 39: 311–318

Hirabayashi Y, Suzki N, Tsuboi M, Endo TA, Toyoda T, Shinga J, Koseki H, Vidal M & Gotoh Y (2009) Polycomb Limits the Neurogenic Competence of Neural Precursor Cells to Promote Astrogenic Fate Transition. *Neuron* 63: 600–613

Isshiki T, Pearson B, Holbrook S & Doe CQ (2001) Drosophila Neuroblasts Sequentially Express Transcription Factors which Specify the Temporal Identity of Their Neuronal Progeny.

Jessell TM (2000) Neuronal specification in the spinal cord: inductive signals and transcriptional codes. *Nat Rev Genet* 1: 20–29

Klemm SL, Shipony Z & Greenleaf WJ (2019) Chromatin accessibility and the regulatory epigenome. *Nat Rev Genet* 20: 207–220

Konstantinides N, Holguera I, Rossi AM, Escobar A, Dudragne L, Chen Y-C, Tran TN, Martínez Jaimes AM, Özel MN, Simon F, *et al* (2022) A complete temporal transcription factor series in the fly visual system. *Nature* 604: 316–322

Kriegstein A & Alvarez-Buylla A (2009) The Glial Nature of Embryonic and Adult Neural Stem Cells.

Li X, Liu G, Yang L, Li Z, Zhang Z, Xu Z, Cai Y, Du H, Su Z, Wang Z, *et al* (2021) Decoding Cortical Glial Cell Development. *Neurosci Bull* 37: 440–460

Li Z, Liu G, Yang L, Sun M, Zhang Z, Xu Z, Gao Y, Jiang X, Su Z, Li X, *et al* (2023)

*BMP7* expression in mammalian cortical radial glial cells increases the length of the neurogenic period. *Protein Cell*: pwad036

Liang XG, Hoang K, Meyerink BL, Kc P, Paraiso K, Wang L, Jones IR, Zhang Y, Katzman S, Finn TS, *et al* (2024) A conserved molecular logic for neurogenesis to gliogenesis switch in the cerebral cortex. *Proc Natl Acad Sci* 121: e2321711121

Lin Y, Yang J, Shen Z, Ma J, Simons BD & Shi S-H (2021) Behavior and lineage progression of neural progenitors in the mammalian cortex. *Curr Opin Neurobiol* 66: 144–157

Merkle FT, Mirzadeh Z & Alvarez-Buylla A (2007) Mosaic Organization of Neural Stem Cells in the Adult Brain. *Science* 317: 381–384

Mita K, Tsuji H, Morimyo M, Takahashi E, Nenoi M, Ichimura S, Yamauchi M, Hongo E & Hayashi A (1995) The human gene encoding the largest subunit of RNA polymerase II. *Gene* 159: 285–286

Miyares RL & Lee T (2019) Temporal control of Drosophila central nervous system development. *Curr Opin Neurobiol* 56: 24–32

Molyneaux BJ, Arlotta P, Menezes JRL & Macklis JD (2007) Neuronal subtype specification in the cerebral cortex. *Nat Rev Neurosci* 8: 427–437

Muralidharan B, Khatri Z, Maheshwari U, Gupta R, Roy B, Pradhan SJ, Karmodiya K, Padmanabhan H, Shetty AS, Balaji C, *et al* (2017) LHX2 Interacts with the NuRD Complex and Regulates Cortical Neuron Subtype Determinants *Fezf2* and *Sox11*. *J Neurosci* 37: 194–203

Namihira M, Kohyama J, Semi K, Sanosaka T, Deneen B, Taga T & Nakashima K (2009) Committed Neuronal Precursors Confer Astrocytic Potential on Residual Neural Precursor Cells. *Dev Cell* 16: 245–255

Narayanan R, Pirouz M, Kerimoglu C, Pham L, Wagener RJ, Kiszka KA, Rosenbusch J, Seong RH, Kessel M, Fischer A, *et al* (2015) Loss of BAF (mSWI/SNF) Complexes Causes Global Transcriptional and Chromatin State Changes in Forebrain Development. *Cell Rep* 13: 1842–1854

Narendra V, Rocha PP, Mazzoni EO & Reinberg D (2015) CTCF establishes discrete

functional chromatin domains at the Hox clusters during differentiation.

Nguyen H, Sokpor G, Parichha A, Pham L, Saikhedkar N, Xie Y, Ulmke PA, Rosenbusch J, Pirouz M, Behr R, *et al* (2022) BAF (mSWI/SNF) complex regulates mediolateral cortical patterning in the developing forebrain. *Front Cell Dev Biol* 10: 1011109

Nitarska J, Smith JG, Sherlock WT, Hillege MMG, Nott A, Barshop WD, Vashisht AA, Wohlschlegel JA, Mitter R & Riccio A (2016) A Functional Switch of NuRD Chromatin Remodeling Complex Subunits Regulates Mouse Cortical Development. *Cell Rep* 17: 1683–1698

Noack F, Vangelisti S, Raffl G, Carido M, Diwakar J, Chong F & Bonev B (2022) Multimodal profiling of the transcriptional regulatory landscape of the developing mouse cortex identifies Neurog2 as a key epigenome remodeler. *Nat Neurosci* 25: 154–167

Noctor SC, Martínez-Cerdeño V, Ivic L & Kriegstein AR (2004) Cortical neurons arise in symmetric and asymmetric division zones and migrate through specific phases. *Nat Neurosci* 7: 136–144

Ochi S, Imaizumi Y, Shimojo H, Miyachi H & Kageyama R (2020) Oscillatory expression of Hes1 regulates cell proliferation and neuronal differentiation in the embryonic brain.

Petryniak MA, Potter GB, Rowitch DH & Rubenstein JLR (2007) Dlx1 and Dlx2 Control Neuronal versus Oligodendroglial Cell Fate Acquisition in the Developing Forebrain. *Neuron* 55: 417–433

Qian X, Shen Q, Goderie SK, He W, Capela A, Davis AA & Temple S (2000) Timing of CNS Cell Generation: A Programmed Sequence of Neuron and Glial Cell Production from Isolated Murine Cortical Stem Cells.

Rakic P (2007) The radial edifice of cortical architecture: From neuronal silhouettes to genetic engineering. *Brain Res Rev* 55: 204–219

Rauluseviciute I, Riudavets-Puig R, Blanc-Mathieu R, Castro-Mondragon JA, Ferenc K, Kumar V, Lemma RB, Lucas J, Chèneby J, Baranasic D, *et al* (2024) JASPAR 2024: 20th anniversary of the open-access database of transcription

factor binding profiles. *Nucleic Acids Res* 52: D174–D182

Rhodes CT, Thompson JJ, Mitra A, Asokumar D, Lee DR, Lee DJ, Zhang Y, Jason E, Dale RK, Rocha PP, *et al* (2022) An epigenome atlas of neural progenitors within the embryonic mouse forebrain. *Nat Commun* 13: 4196

Ruan X, Kang B, Qi C, Lin W, Wang J & Zhang X (2021) Progenitor cell diversity in the developing mouse neocortex. *Proc Natl Acad Sci* 118: e2018866118

Samanta J & Kessler JA (2004) Interactions between ID and OLIG proteins mediate the inhibitory effects of BMP4 on oligodendroglial differentiation. *Development* 131: 4131–4142

Sanosaka T, Imamura T, Hamazaki N, Chai M, Igarashi K, Ideta-Otsuka M, Miura F, Ito T, Fujii N, Ikeo K, *et al* (2017) DNA Methylome Analysis Identifies Transcription Factor-Based Epigenomic Signatures of Multilineage Competence in Neural Stem/Progenitor Cells. *Cell Rep* 20: 2992–3003

Sansom SN, Griffiths DS, Faedo A, Kleinjan D-J, Ruan Y, Smith J, van Heyningen V, Rubenstein JL & Livesey FJ (2009) The Level of the Transcription Factor Pax6 Is Essential for Controlling the Balance between Neural Stem Cell Self-Renewal and Neurogenesis. *PLoS Genet* 5: e1000511

Saunders A, Macosko EZ, Wysoker A, Goldman M, Krienen FM, de Rivera H, Bien E, Baum M, Bortolin L, Wang S, *et al* (2018) Molecular Diversity and Specializations among the Cells of the Adult Mouse Brain. *Cell* 174: 1015-1030.e16

Shen Z, Lin Y, Yang J, Jörg DJ, Peng Y, Zhang X, Xu Y, Hernandez L, Ma J, Simons BD, *et al* (2021) Distinct progenitor behavior underlying neocortical gliogenesis related to tumorigenesis. *Cell Rep* 34: 108853

Silbereis JC, Nobuta H, Tsai H-H, Heine VM, McKinsey GL, Meijer DH, Howard MA, Petryniak MA, Potter GB, Alberta JA, *et al* (2014) Olig1 Function Is Required to Repress Dlx1/2 and Interneuron Production in Mammalian Brain. *Neuron* 81: 574–587

Takizawa T, Nakashima K, Namihira M, Ochiai W, Uemura A, Yanagisawa M, Fujita N, Nakao M & Taga T (2001) DNA Methylation Is a Critical Cell-Intrinsic

Determinant of Astrocyte Differentiation in the Fetal Brain. *Dev Cell* 1: 749–758

Taylor MK, Yeager K & Morrison SJ (2007) Physiological Notch signaling promotes gliogenesis in the developing peripheral and central nervous systems. *Development* 134: 2435–2447

Telley L, Agirman G, Prados J, Amberg N, Fièvre S, Oberst P, Bartolini G, Vitali I, Cadilhac C, Hippenmeyer S, *et al* (2019) Temporal patterning of apical progenitors and their daughter neurons in the developing neocortex. *Science* 364: eaav2522

Tuoc TC, Radyushkin K, Tonchev AB, Pinon MC, Ashery-Padan R, Molnar Z, Davidoff MS & Stoykova A (2009) Selective Cortical Layering Abnormalities and Behavioral Deficits in Cortex-Specific Pax6 Knock-Out Mice. *J Neurosci* 29: 8335–8349

Ventura F (2013) BMP signaling in telencephalic neural cell specification and maturation. *Front Cell Neurosci*

Vorontsov IE, Eliseeva IA, Zinkevich A, Nikonov M, Abramov S, Boytsov A, Kamenets V, Kasianova A, Kolmykov S, Yevshin IS, *et al* (2024) HOCOMOCO in 2024: a rebuild of the curated collection of binding models for human and mouse transcription factors. *Nucleic Acids Res* 52: D154–D163

Waclaw RR, Wang B, Pei Z, Ehrman LA & Campbell K (2009) Distinct Temporal Requirements for the Homeobox Gene Gsx2 in Specifying Striatal and Olfactory Bulb Neuronal Fates. *Neuron* 63: 451–465

Weirauch MT, Yang A, Albu M, Cote AG, Montenegro-Montero A, Drewe P, Najafabadi HS, Lambert SA, Mann I, Cook K, *et al* (2014) Determination and Inference of Eukaryotic Transcription Factor Sequence Specificity. *Cell* 158: 1431–1443

Wiles ET & Selker EU (2017) H3K27 methylation: a promiscuous repressive chromatin mark. *Curr Opin Genet Dev* 43: 31–37

Winkler CC, Yabut OR, Fregoso SP, Gomez HG, Dwyer BE, Pleasure SJ & Franco SJ (2018) The Dorsal Wave of Neocortical Oligodendrogenesis Begins

Embryonically and Requires Multiple Sources of Sonic Hedgehog. *J Neurosci* 38: 5237–5250

Wu Y, Liu Y, Levine EM & Rao MS (2003) Hes1 but not Hes5 regulates an astrocyte versus oligodendrocyte fate choice in glial restricted precursors. *Dev Dyn* 226: 675–689

Yang L, Li Z, Liu G, Li X & Yang Z (2022) Developmental Origins of Human Cortical Oligodendrocytes and Astrocytes. *Neurosci Bull* 38: 47–68

Zhan X, Shi X, Zhang Z, Chen Y & Wu JI (2011) Dual role of Brg chromatin remodeling factor in Sonic hedgehog signaling during neural development. *Proc Natl Acad Sci* 108: 12758–12763

Zhang Y, Liu G, Guo T, Liang XG, Du H, Yang L, Bhaduri A, Li X, Xu Z, Zhang Z, *et al* (2020) Cortical Neural Stem Cell Lineage Progression Is Regulated by Extrinsic Signaling Molecule Sonic Hedgehog. *Cell Rep* 30: 4490-4504.e4

Zhou Q & Anderson DJ (2002) The bHLH Transcription Factors OLIG2 and OLIG1 Couple Neuronal and Glial Subtype Specification. *Cell* 109: 61–73

Zhou Q, Choi G & Anderson DJ (2001) The bHLH Transcription Factor Olig2 Promotes Oligodendrocyte Differentiation in Collaboration with Nkx2.2. *Neuron* 31: 791–807

Zhou Y, Song WM, Andhey PS, Swain A, Levy T, Miller KR, Poliani PL, Cominelli M, Grover S, Gilfillan S, *et al* (2020) Human and mouse single-nucleus transcriptomics reveal TREM2-dependent and TREM2-independent cellular responses in Alzheimer's disease. *Nat Med* 26: 131–142

Zhuo L, Sun B, Zhang C-L, Fine A, Chiu S-Y & Messing A Live Astrocytes Visualized by Green Fluorescent Protein in Transgenic Mice.

Zhuo L, Theis M, Alvarez-Maya I, Brenner M, Willecke K & Messing A (2001) hGFAP-cre transgenic mice for manipulation of glial and neuronal function in vivo.

## Figures legends

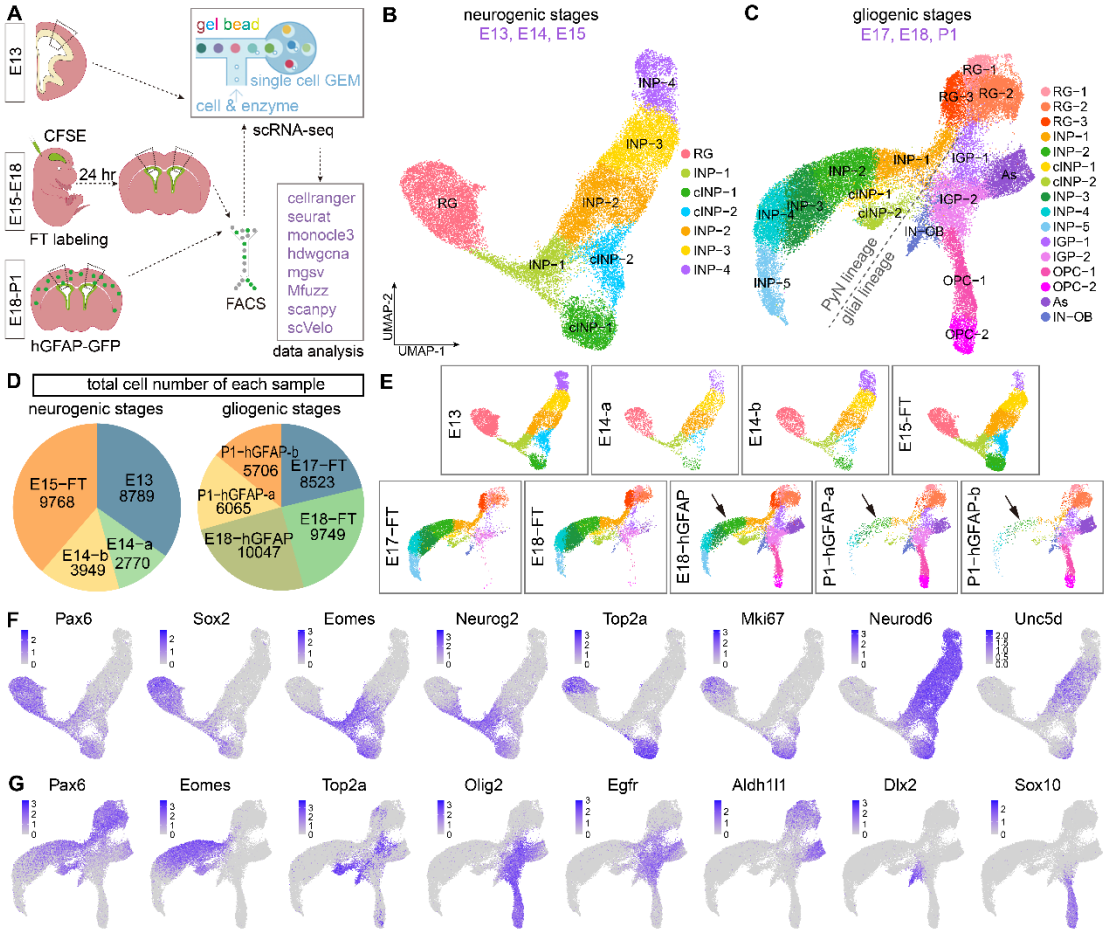


Fig. 1: **Time series scRNA-seq of the developing cortex. A**: Experimental scheme for the time series scRNA-seq analysis of the developing cortex. **B-C**: UMAP projections of the combined scRNA-seq data from neurogenic stages (E13, E14 and E15) and from the gliogenic stages (E17, E18 and P1). RG, radial glia; INP, intermediate neuronal progenitor; cINP, cycling INP; IGP, intermediate glial progenitor; As, astrocyte; OPC, oligodendrocyte precursor cell; IN-OB, OB interneuron. **D**: Total cell number for each individual sample. **E**: UMAP visualization of each sample, with arrows indicating PyN lineage cells. **F-G**: Feature plots of typical cell type markers.

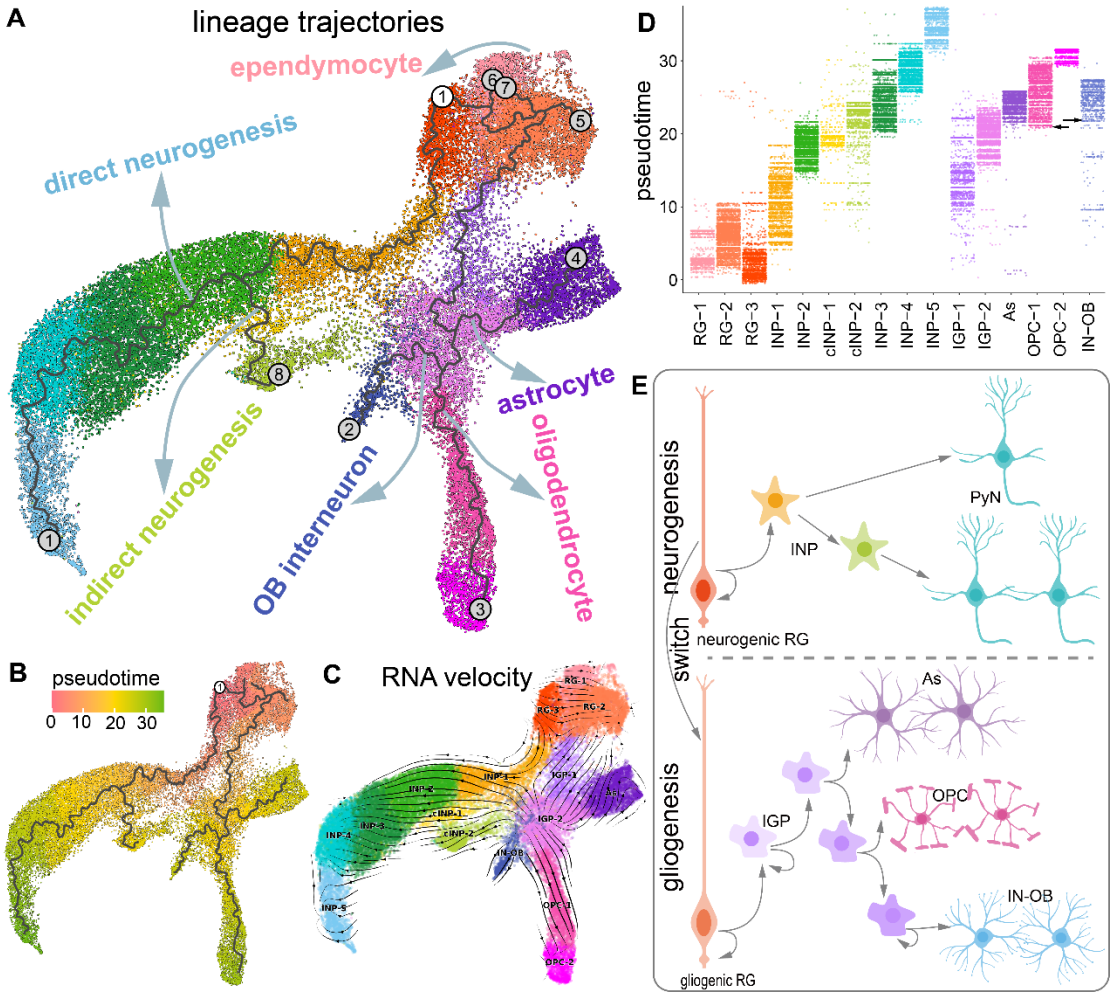


Fig. 2: **Inference of cell lineage trajectories from the gliogenic scRNA-seq dataset**. **A**: Cell lineage trajectories recovered from the gliogenic scRNA-seq dataset. The two primary trajectories correspond to neurogenesis and gliogenesis. The number 1 on a white background denotes the root cells, while numbers on a gray background indicate the tip cells. **B**: UMAP visualization of the inferred pseudotime. **C**: Lineage trajectories as determined by RNA velocity analysis. **D**: Pseudotime values for individual cell types. **E**: Schematic diagram of cortical cellular diversification.

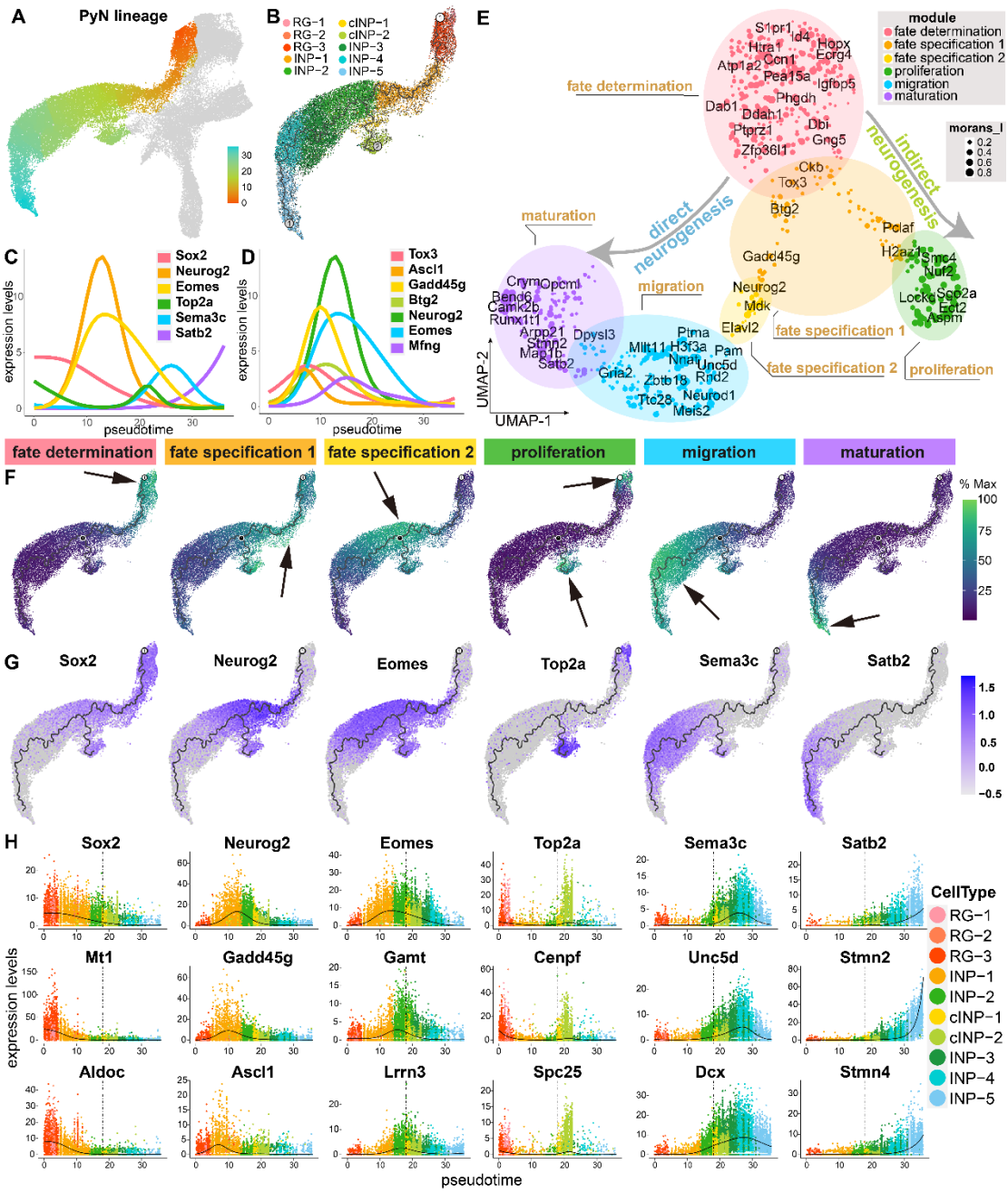


Fig. 3: **Molecular maps illustrating PyN lineage commitment**. **A-B**: UMAP visualization of glial lineage cells, colored by pseudotime (**A**) and cell types (**B**). **C-D**: Gene expression levels along PyN lineage pseudotime, colored by genes. Representative genes with peak expression at different pseudotime (**C**) and at the PyN fate specification stage (**D**). **E**: A panoramic molecular map of PyN lineage commitment, colored by gene modules. morans_I, spatial autocorrelation Moran's index. **F**: UMAP visualization showing aggregated expression levels for each gene module. **G**: UMAP visualization of representative genes of each gene module. **H**: Gene expression levels along PyN lineage pseudotime, colored by cell types. Cells are ordered by

pseudotime, with a solid line representing the GAM fit of expression levels. The vertical dashed line marks the pseudotime corresponding to the branch point between direct and indirect neurogenesis. Genes within the same module exhibit similar expression patterns.

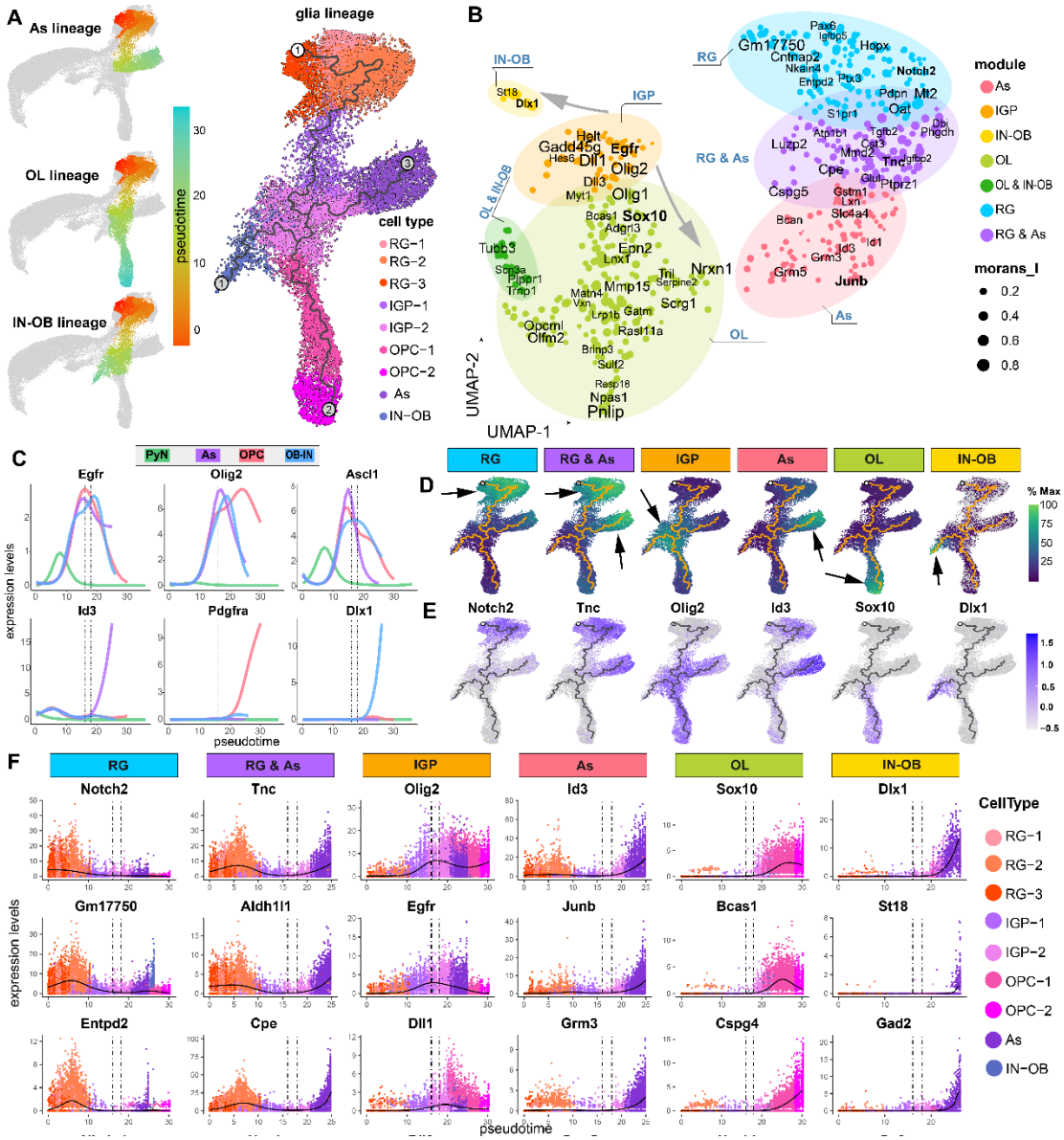


Fig. 4: **Molecular Maps Depicting Glia Lineage Diversification. A**: UMAP visualization of the glial lineage cells, colored by pseudotime (left) and cell types (right). **B**: A panoramic molecular map of glia lineage diversification, colored by gene modules. OL, oligodendrocyte. **C**: Pseudotime dynamic genes with peak expression in the IGPs (upper) and those with lineage-biased expression (lower), colored by cell lineages. **D**: UMAP visualization showing aggregated expression levels for each individual gene module. **E**: UMAP visualization of representative genes from each

gene module. **F**: Gene expression levels along glia lineage pseudotime.

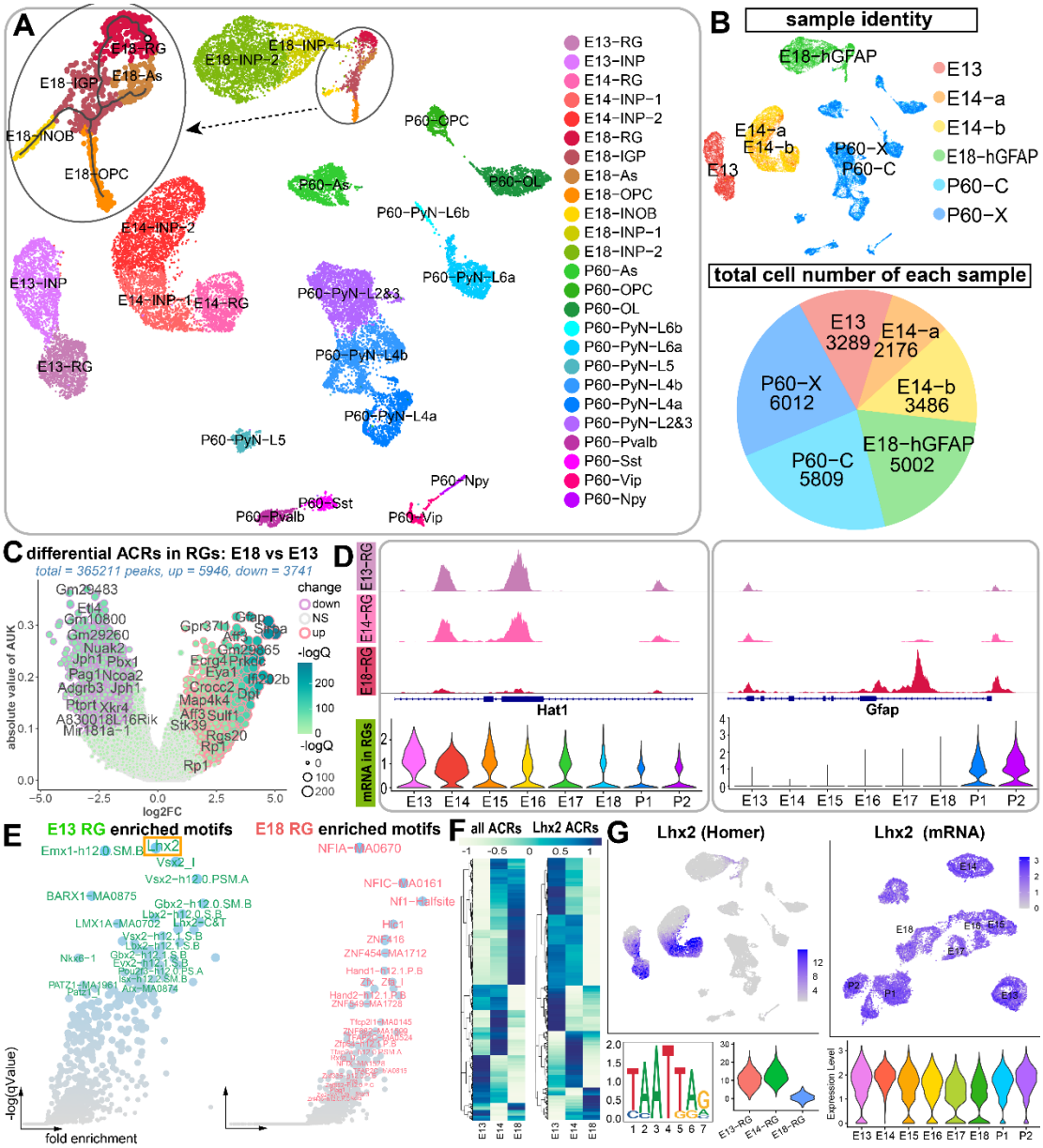


Fig. 5: **Time-Series snATAC-seq Analysis of Developing Cortex. A**: UMAP projections of the combined snATAC-seq dataset encompassing embryonic and adult stages (E13, E14, E18, and P60). The circled area highlights lineage trajectories of E18 hGFAP-GFP glia. *Sst*, Somatostatin interneuron; *Pvalb*, Parvalbumin interneuron; *Npy*, Neuropeptide Y interneuron; *Vip*, Vasoactive Intestinal Peptide interneuron; L2-6, cortical layers 2-6. **B**: UMAP visualization of sample identities (upper) and pie chart showing total cell number in individual samples (lower). **C**: Differential ATAC-peak analysis between E13 and E18 RGs. AUK, area under the Kappa curve; log2FC, $\log_2$(fold change); -logQ, $-\log_{10}$(q-value). **D**: Representative early and late RG specific peaks (upper) and corresponding mRNA expression levels in cortical RGs (lower). **E**: Motifs enriched on E13 versus E18 RG specific ACRs. **F:**

Heat maps showing the temporal changes in chromatin accessibility in cortical RGs. Notably, the majority of ACRs containing Lhx2 binding motifs exhibit reduced accessibility over time (Right). **G**: Lhx2 motif activity (left), mRNA expression levels in cortical RGs (right).

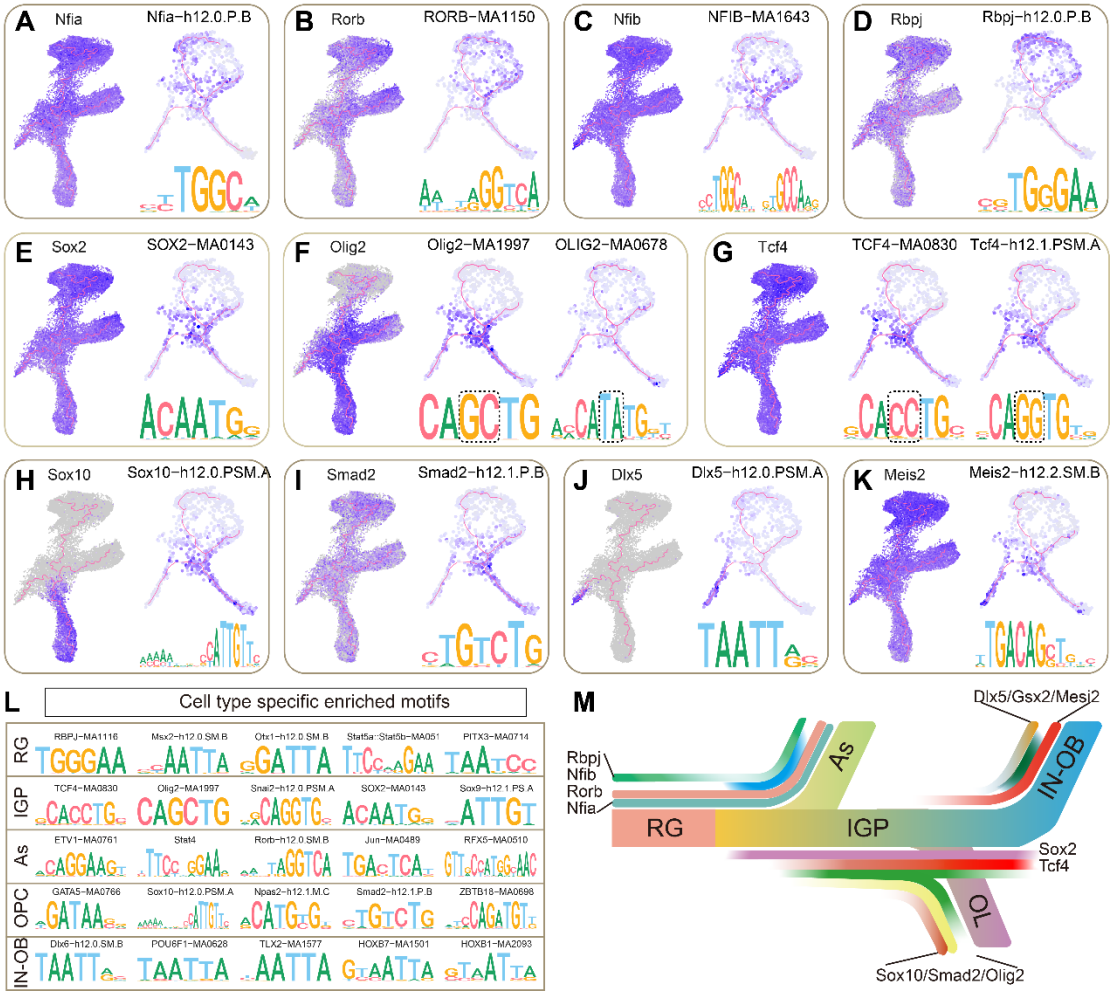


**Fig. 6: Dynamic transcription factor motif activities along glial lineage cells. A-K:** A comparison of gene expression pattern with its corresponding motif activity in glial lineage cells. In each panel, **left**: mRNA expression levels of representative genes in glial lineage cells; **right**: motif activities of the corresponding transcription factors in glial lineage cells. Pink lines represent cell lineage trajectories reconstructed using Monocle3. **L:** Top overrepresented motifs for each cell type identified from the glial lineage cells in the E18 snATAC-seq data. **M:** Schematic diagram illustrating transcription factor activities along the glial lineage.

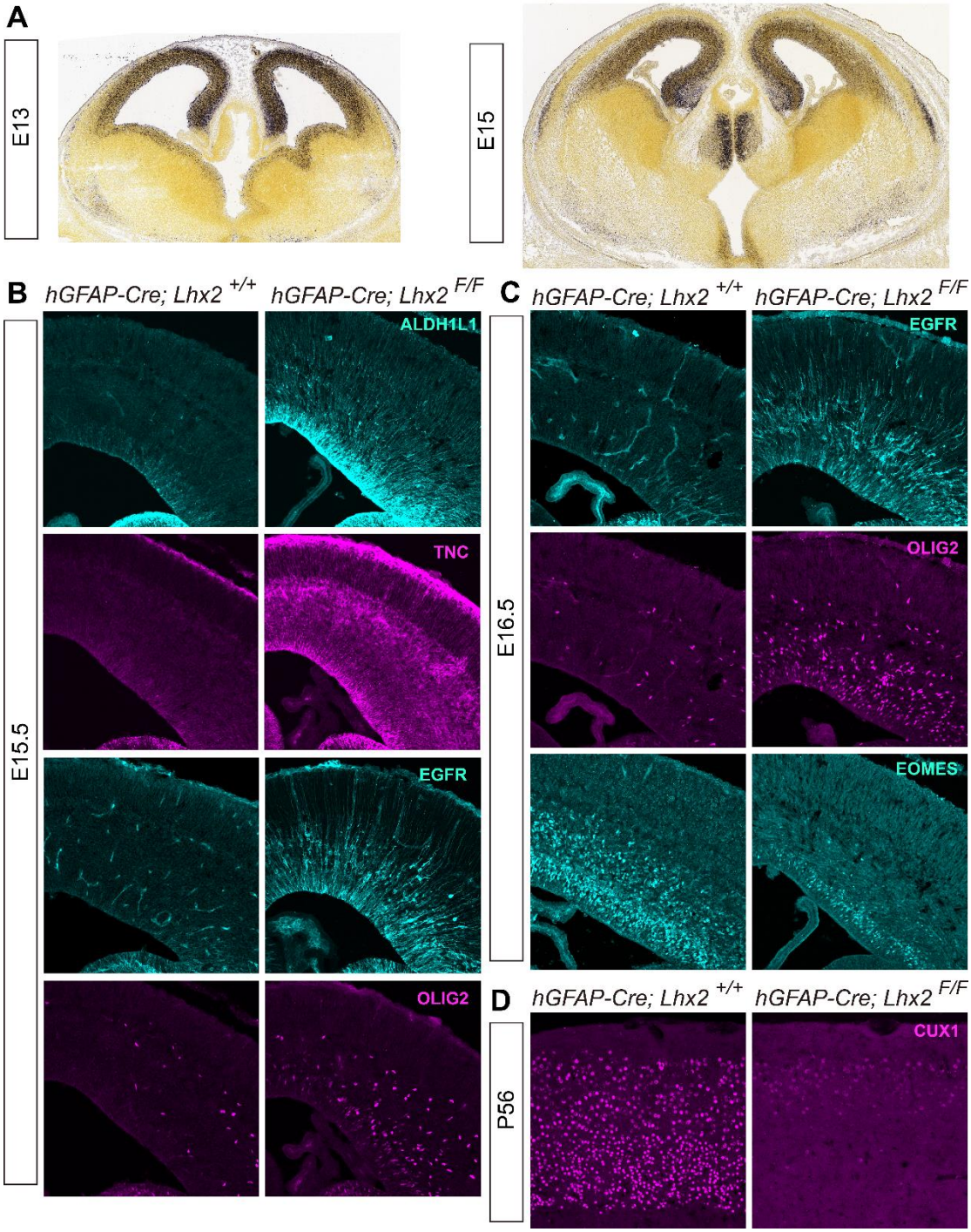


Fig. 7: **Lhx2 inactivation leads to premature gliogenesis at the expense of upper-layer PyNs. A:** *In situ* hybridization of *Lhx2* in the embryonic brain (Allen Brain Atlas). **B:** Immunostaining of ALDH1L1, TNC, EGFR, and OLIG2 in E15.5 control and *Lhx2* cKO cortices. **C:** Immunostaining of EGFR, OLIG2, and EOMES in E16.5 control and *Lhx2* cKO cortices. **D:** Immunostaining of CUX1 in P56 control and *Lhx2* cKO cortices.

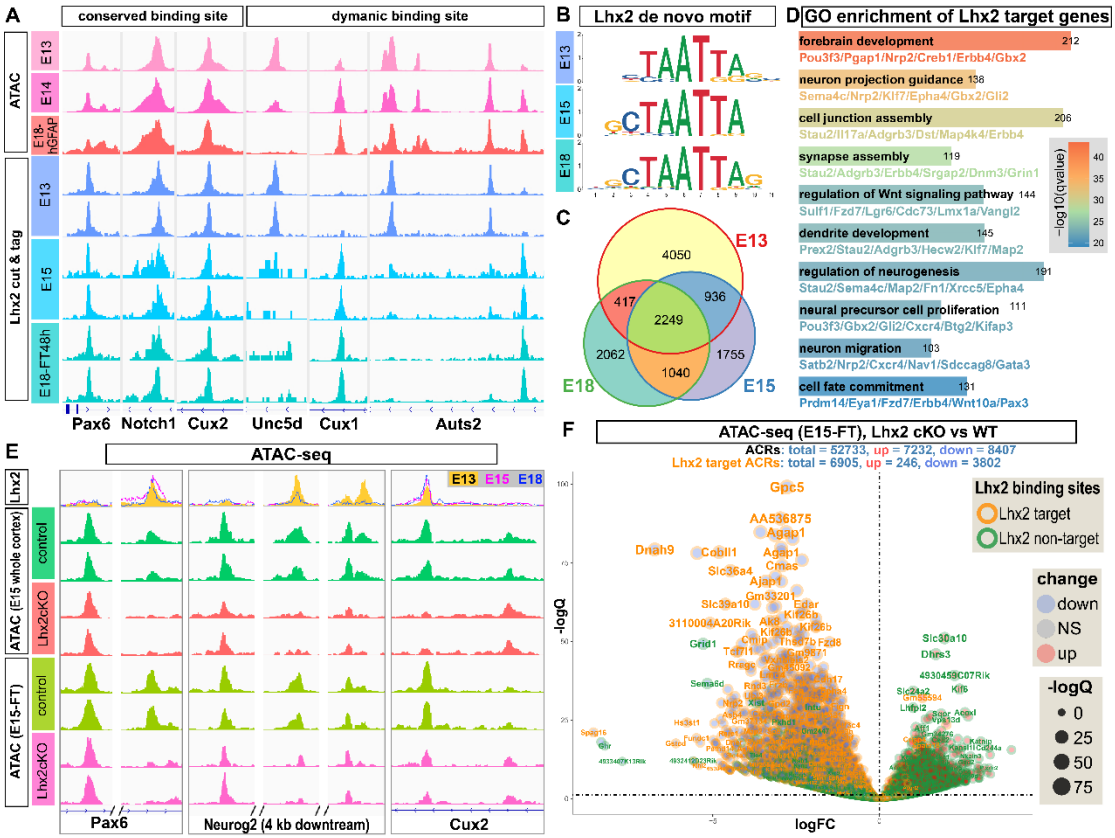


Fig. 8: **Lhx2 temporally binds to distinct genes to maintain chromatin accessibility**. **A**: The consensus and timepoints specific Lhx2 CUT&Tag-seq peaks. **B**: De novo motifs identified from E13, E15, and E18 Lhx2 CUT&Tag-seq. **C**: Venn diagram showing consensus and specific Lhx2 binding sites across E13, E15, and E18 cortical progenitors. **D**: GO enrichment analysis of Lhx2 target genes. **E**: ATAC-seq peaks in E15 control and Lhx2 cKO cortices. Lhx2 target ACRs were indicated by Lhx2 CUT&Tag-seq. **F**: Differential ATAC-peak analysis between E15 control and Lhx2 cKO cortical progenitors, colored by Lhx2 target/non-target ACRs.

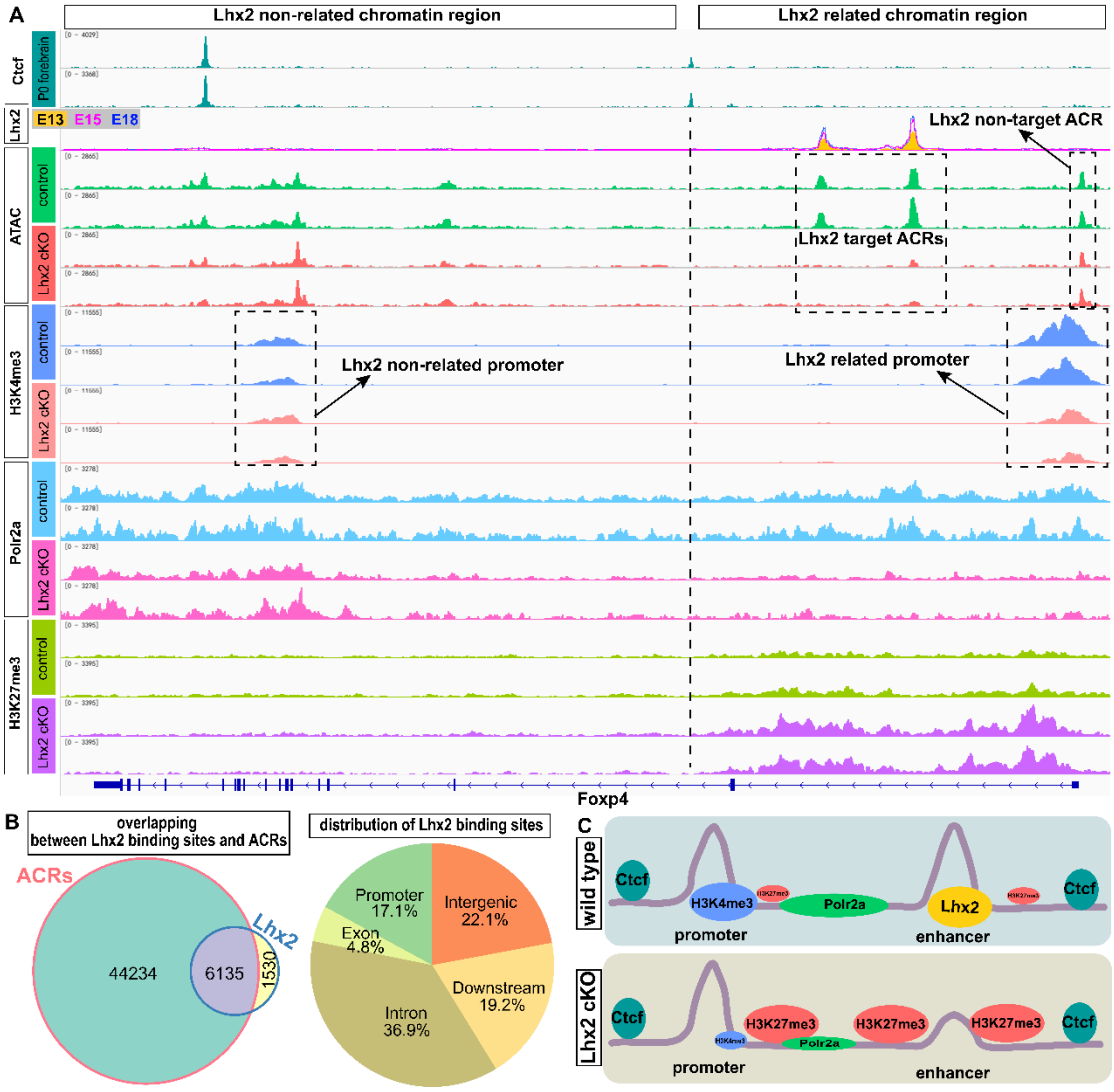


Fig. 9: **Lhx2 Inactivation Leads to Epigenetic Repression of Target Genes. A**: Enrichment of H3K4me3, H3K27me3, and Polr2a at the *Foxp4* locus in *control* and *Lhx2 cKO* cortices. The dashed line indicates the boundary between Lhx2-related and non-related chromatin regions. **B**: A Venn diagram showing the overlap between Lhx2 binding sites and ACRs (left), and a pie chart showing fractional distribution of Lhx2 binding sites (right). **C**: Schematic diagram illustrating the epigenetic repression induced by *Lhx2* inactivation.

## Tables

**Table S1:** Marker genes of each scRNA-seq cell type. The sheet “neurogenic” and “gliogenic” related to Fig. 1. The sheet ‘RG2vsRG3’ related to Fig. S2A-D.

**Table S2:** Gene modules of the PyN and glia lineages. Related to Fig. 3 and Fig. 4.

**Table S3:** Temporal dynamic gene expression in cortical RGs. Related to Fig. S2D-E.

**Table S4:** Cell type specific ACRs and motif activities across the snATAC-seq clusters. The sheet “clusterMarker” related to Fig. 5A and Fig. S4A. The sheet “RG_E18vsE13” related to Fig. 5c-d. The sheet “TFactivity” related to Fig. 5E and Fig. S4B.

**Table S5:** scRNA-seq on control and *Lhx2*-cKO cortical progenitors. The sheet “allCluster” related to Fig. 7G-K. The sheet “RG” related to Fig. S5B-E.

**Table S6:** Peaks of *Lhx2* CUT&Tag-seq on E13, E15 and E18 cortical progenitors. Related to Fig. 8A-C.

**Table S7:** Differential ATAC-peak analysis between E15 control and *Lhx2*-cKO cortical progenitors. Related to Fig. 8E-F.

**Table S8:** Differential peak analysis for H3K4me3, HeK27me3 and POLR2A CUT&Tag-seq on E15 control and *Lhx2*-cKO cortices. Related to Fig. 9A.

## Expanded View Figure legends

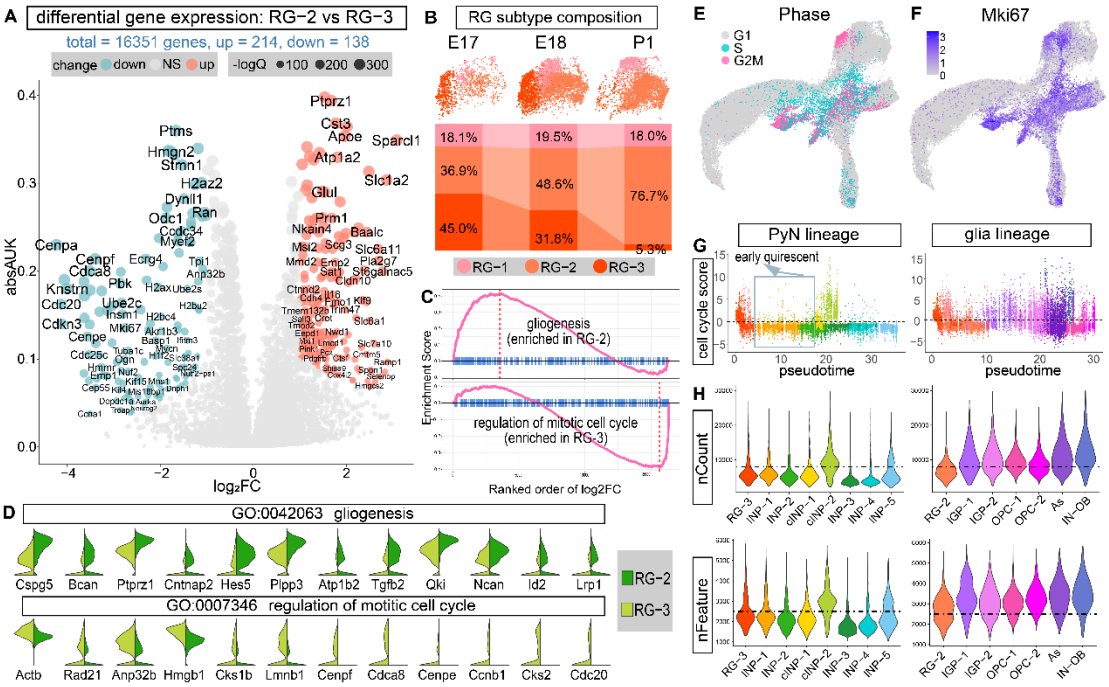


Fig. S1: **Differential Gene Expression Between Neurogenic and Gliogenic Progenitors of the Gliogenic scRNA-seq Dataset. A**: Differential gene expression analysis between RG-2 and RG-3. **B**: Composition of RG subtypes at each timepoint. **C**: Enrichment of GO term “gliogenesis” in RG-2 and “cell cycle” in RG-3. **D**: Split violin plots of genes differentially expressed between RG-2 and RG-3. **E**: UMAP visualization of cell cycle phase identities. **F**: Feature plot of cell cycle gene *Mki67*. **G**: Cell cycle scores along the PyN lineage pseudotime (left) and the glia lineage pseudotime (right), colored by cell types. **H**: Total mRNA counts and total genes counts per cell in each cell type, ordered by pseudotime.

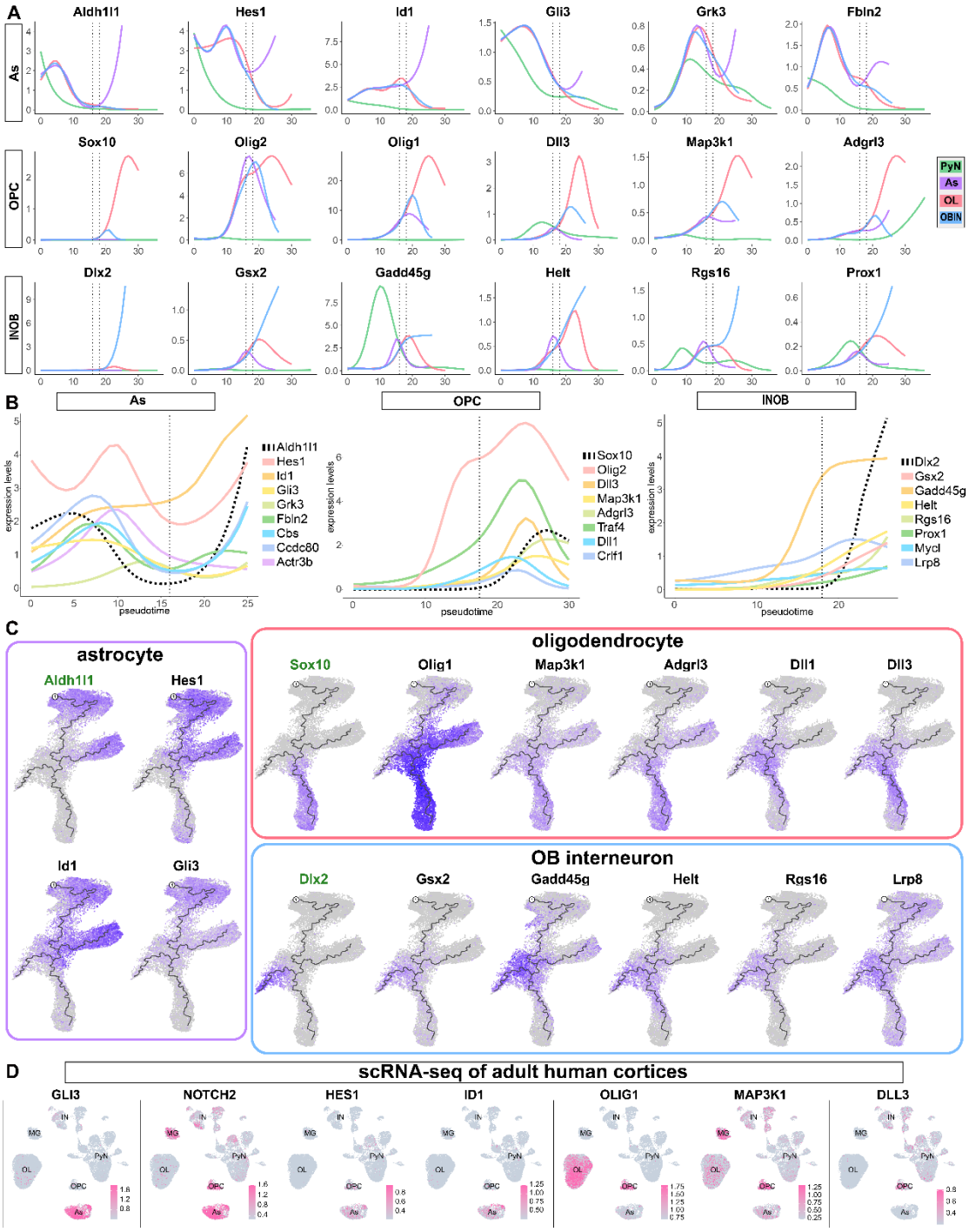


Fig. S2: **Putative Lineage Driver Genes of Astrocytes, Oligodendrocytes, and OB Interneurons. A**: Gene expression levels along each lineage pseudotime, colored by lineages. Putative lineage driver genes are selectively expressed in a particular lineage. The dashed vertical lines indicate the pseudotime corresponding to the branch points. **B**: Gene expression levels along a specific lineage pseudotime, colored by genes. Putative lineage driver genes are expressed earlier than the marker genes of each lineage (black dashed line). **C**: Expression of Lineage marker

genes (green gene names) and lineage driver genes (black gene names) along the glial lineage trajectories. **D**: The putative lineage driver genes are specifically expressed in the corresponding cell types of adult human cortices.

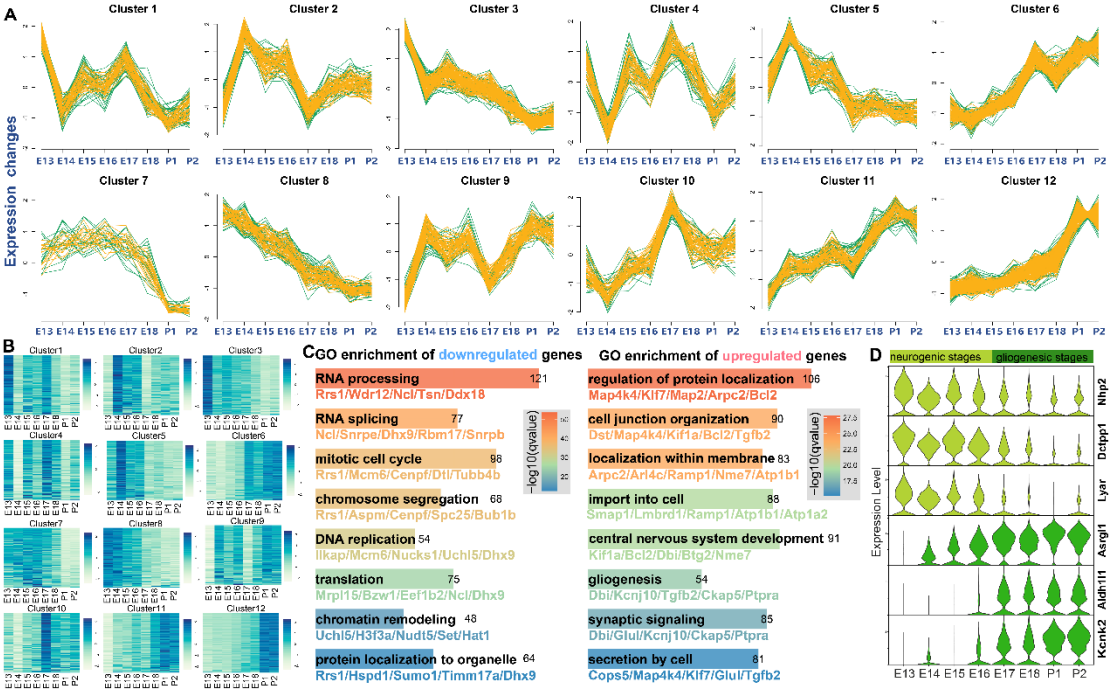


Fig. S3: **Temporal Dynamics of Gene Expression in Cortical RGs**. **A**: Clustering of the dynamic patterns of temporal gene expression levels in cortical RGs. **B**: Heatmap plotting of gene expression levels for each gene cluster, colored by average relative counts. **C**: GO enrichment analysis of temporally downregulated (left) and upregulated (right) genes. **D**: Violin plots showing genes primarily expressed in RGs during neurogenic (light green) and gliogenic (dark green) stages.

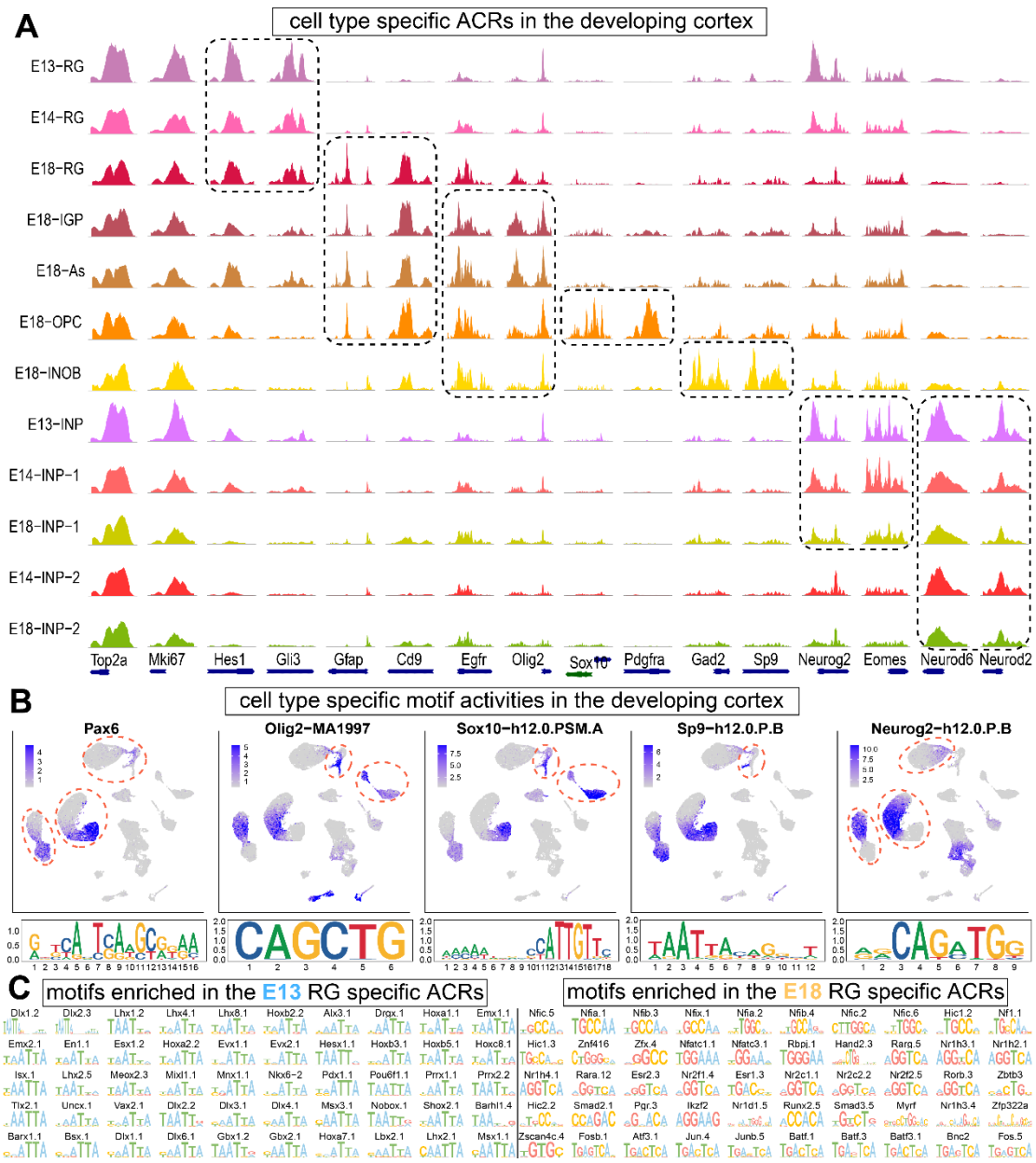


Fig. S4: **Cell-Type-Specific Chromatin Accessibility and Transcription Factor Motif Activities.** **A**: snATAC-seq coverage plots showing cell type specific chromatin accessibility during embryonic cortical development, colored by cell types. **B**: UMAP visualization of transcription factor motif activities. The circled areas indicate specific motif activities in the corresponding cell type. **C**: Overrepresented motifs in peaks that are differentially accessible between E13 and E18 RGs. While the overrepresented motifs in E13 RG specific peaks are AT-rich, it was GC-rich in E18 RG specific peaks.

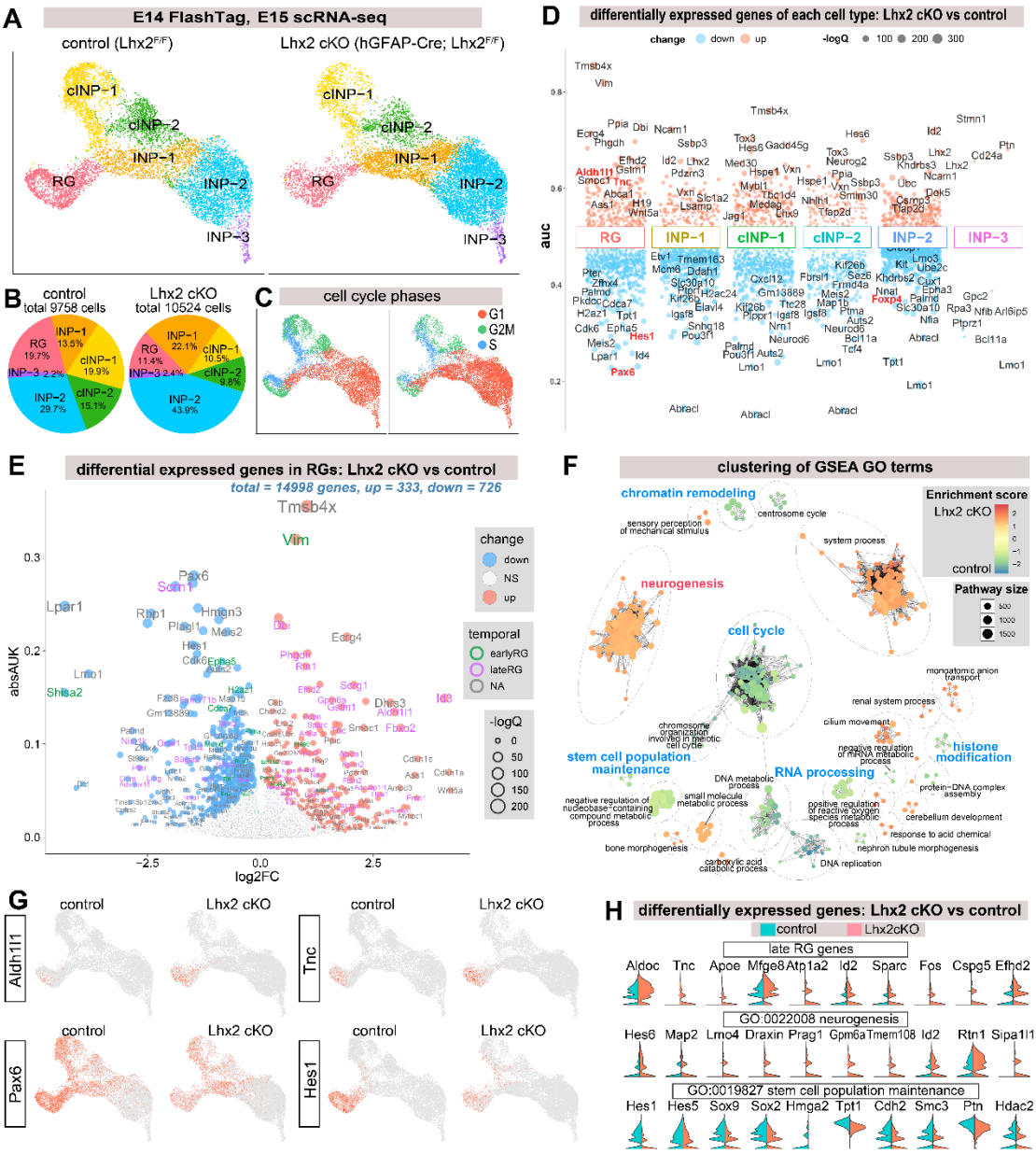


Fig. S5: **scRNA-seq analysis of FT/FACS-sorted cortical progenitors from control and Lhx2 cKO mice. A**: UMAP projections of the combined scRNA-seq data from control or Lhx2 cKO cortical progenitors, colored by cell types. **B**: Comparison of cell type composition between control and Lhx2 cKO mice. **C**: UMAP plot shwoing cell cycle phase identities. **D**: Differential gene expression analysis for each cell type between control and Lhx2 cKO mice. **E**: Differential gene expression between control and *Lhx2*-cKO cortical RGs. Many late-stage RG genes (purple) are predominantly upregulated in cortical RGs upon *Lhx2* inactivation. **F**: Clustering of GSEA GO terms that enriched in control and Lhx2-cKO RGs, colored by enrichment scores. Lower enrichment scores indicate GO term enrichment in control RGs, while higher scores indicate enrichment in *Lhx2*-cKO RGs. Each dot representing a GO term and similar

GO terms are grouped into clusters. **G**: Representative differentially expressed genes between control and Lhx2 cKO mice. **H**: Split violin plots illustrating differential gene expression between control and *Lhx2* cKO RGs.